



# Interplay between magnetic excitations and plasticity in body-centered cubic chromium

Baptiste Bienvenu, Chu Chun Fu, Emmanuel Clouet

## ► To cite this version:

Baptiste Bienvenu, Chu Chun Fu, Emmanuel Clouet. Interplay between magnetic excitations and plasticity in body-centered cubic chromium. *Physical Review B*, 2023, 107, pp.134105. 10.1103/PhysRevB.107.134105 . cea-04272000

**HAL Id: cea-04272000**

**<https://cea.hal.science/cea-04272000v1>**

Submitted on 6 Nov 2023



**HAL** is a multi-disciplinary open access archive for the deposit and dissemination of scientific research documents, whether they are published or not. The documents may come from teaching and research institutions in France or abroad, or from public or private research centers.

L'archive ouverte pluridisciplinaire **HAL**, est destinée au dépôt et à la diffusion de documents scientifiques de niveau recherche, publiés ou non, émanant des établissements d'enseignement et de recherche français ou étrangers, des laboratoires publics ou privés.



Distributed under a Creative Commons Attribution 4.0 International License

## Interplay between magnetic excitations and plasticity in body-centered cubic chromium

Baptiste Bienvenu , Chu Chun Fu, and Emmanuel Clouet <sup>\*</sup>*Université Paris-Saclay, CEA, Service de Recherches de Métallurgie Physique, F-91191 Gif-sur-Yvette, France*

(Received 17 November 2022; revised 16 March 2023; accepted 21 March 2023; published 6 April 2023)

The effect of finite-temperature magnetic excitations on the plasticity of body-centered cubic chromium is studied. In chromium, the magnetic order is disrupted by the  $\frac{1}{2}\langle 111 \rangle$  Burgers vectors of dislocations, creating magnetic frustrations partially resolved through the generation of magnetic faults. These faults may bear consequences on plasticity, the controlling parameter being their energy. Through the inclusion of finite-temperature magnetic excitations, we show in this work that these faults vanish below the Néel temperature, thus leaving  $\frac{1}{2}\langle 111 \rangle$  dislocations free to move. When the faults have disappeared, complex noncollinear magnetic structures are stabilized, surrounding the region sheared by these dislocations, with a negligible excess magnetic energy.

DOI: [10.1103/PhysRevB.107.134105](https://doi.org/10.1103/PhysRevB.107.134105)

## I. INTRODUCTION

Chromium (Cr) is a body-centered cubic (bcc) transition metal with a magnetic order close to antiferromagnetic (AF) below ambient temperature, namely, a quasiperiodic modulation of the magnetic moments along a  $\langle 100 \rangle$  axis of the crystal with a local AF order, called a spin-density wave (SDW) [1]. With increasing temperature, magnetic fluctuations gradually lead to the disappearance of long-range magnetic order, with the paramagnetic (PM) phase appearing above the Néel temperature  $T_N = 311$  K [2,3]. In this temperature range, the motion of dislocations in Cr transitions from the Peierls mechanism, governed by lattice friction, to an athermal regime where lattice friction vanishes [4], thus raising the question about the interplay between magnetic excitations and plasticity at finite temperature.

Through comparison of the properties of  $\frac{1}{2}\langle 111 \rangle$  screw dislocations predicted using *ab initio* calculations in the two nonmagnetic (NM) and AF phases, it was concluded in previous studies [5,6] that the main impact of magnetism on the plasticity of bcc Cr is the generation of magnetic faults caused by the disruption of the magnetic order by the  $\frac{1}{2}\langle 111 \rangle$  Burgers vector of these dislocations. Due to the energy of such a magnetic fault,  $\frac{1}{2}\langle 111 \rangle$  dislocations might be forced to coexist and move pairwise, creating  $\langle 111 \rangle$  superdislocations corresponding to two  $\frac{1}{2}\langle 111 \rangle$  dislocations bounding a magnetic fault. But the existence of such  $\langle 111 \rangle$  superdislocation still requires experimental validation. Such a pairing of dislocations was previously proposed by Marcinkowski and Lipsitt [4], and is responsible for a magnetic strengthening caused by the added friction due to the motion of the fault, its energy controlling the magnitude of this effect. Using the fault energy calculated by *ab initio* calculations at 0 K,  $\gamma = 16$  meV/Å<sup>2</sup> [5], a dissociation distance of about 6 nm is predicted for the superdislocation, leading to an added friction stress of about 25 MPa impeding their motion. No experimental evidence of

such strengthening was, however, reported close to  $T_N$  [4], possibly indicating the weak energy of the fault at these temperatures. Therefore, a decrease of the fault energy is expected from its 0-K value up to  $T_N$ , where the magnetic fault might have a negligible cost. Additionally, recent transmission electron microscope (TEM) observations at room temperature of specimens compressed at 77 K [7] did not reveal the presence of such paired  $\frac{1}{2}\langle 111 \rangle$  dislocations, which might not exist in this temperature range.

So far, the impact of magnetism on the plasticity of bcc Cr has only been discussed at 0 K. In an attempt to rationalize these observations, we study in this work the interplay between magnetism and plasticity of bcc Cr at finite temperature, below and above the Néel temperature  $T_N$ . A particular focus is made on the magnetic fault, identified as the main impact of magnetism on Cr plasticity at 0 K, studying its behavior at finite temperature. Starting from the development of a magnetic interaction model based on *ab initio* calculations, we then study magnetic excitations in Cr through sampling of equilibrium configurations found at finite temperature with Metropolis Monte Carlo simulations. We then focus on the bulk magnetic properties of Cr and the transition to the PM phase, before moving on to the stability and energetics of magnetic frustrations caused by a rigid  $\frac{1}{2}\langle 111 \rangle$  shearing and by dislocations.

## II. ENERGETIC MODELS AND SIMULATION TOOLS

Different energetic models are used for studying magnetic properties of bcc Cr from 0 K to finite temperature: *ab initio* calculations and a magnetic Heisenberg-Landau interaction model developed specifically for this work.

A. *Ab initio* calculations

All *ab initio* calculations reported here were performed within density-functional theory (DFT) using the VASP code [8]. A projector augmented wave pseudopotential was used to model Cr, including 12 valence electrons, with the

<sup>\*</sup>emmanuel.clouet@cea.fr

exchange-correlation potential approximated using the GGA-PBE functional [9]. A plane-wave basis with a cutoff energy of 500 eV was used, and the Brillouin zone was sampled with a  $k$ -point mesh centered on  $\Gamma$  with 20 points per inverse lattice parameter unit length in all simulation cells.

Since Cr has an ordered magnetic ground state in the form of a SDW [1], magnetism must be included in all calculations. As already thoroughly discussed in previous studies [5,10–12], DFT calculations predict an AF magnetic ground state instead of this SDW phase. However, we showed in our previous work [5] that this complex SDW phase is well approximated by the AF phase based on their close magnetic orders, energetics, and elastic properties. Magnetism is treated within spin-polarized DFT in the collinear approximation. Constrained magnetism calculations are performed, when necessary, to impose nonequilibrium magnetic moments on atoms [13].

Noncollinear spin-polarized DFT calculations have also been performed to confirm the noncollinear magnetic structures predicted by the Heisenberg-Landau interaction model. These calculations include spin-orbit coupling to incorporate the dependence of the magnetic moments on crystallographic directions. As shown in Table II, collinear and noncollinear DFT calculations lead to the same equilibrium magnetic moment in the AF phase of Cr, the same excess energy of the NM and SDW phases, and the same energy for a magnetic fault lying in a {110} or a {112} plane of the AF phase.

## B. Generalized Heisenberg model

We present in this section an effective magnetic interaction model, used in the following to sample finite-temperature magnetic excitations with a Metropolis spin Monte Carlo sampling, where the spin subsystem is studied on a rigid fixed lattice. As described below, two different sets of parameters are defined for this magnetic model: Set1 which perfectly reproduces *ab initio* calculations, and Set2 which gives a better estimate of the experimental Néel temperature.

### 1. Model and parametrization

Let us consider a magnetic system of  $N$  atoms located at fixed lattice sites  $i$ , each site having a magnetic moment  $\vec{m}_i$ . The Heisenberg-Landau (HL) Hamiltonian of the system, only including magnetic contributions, is [14]<sup>1</sup>

$$E^{\text{mag}}(\{\vec{m}_i\}) = \sum_{i=1}^N \left[ A \|\vec{m}_i\|^2 + B \|\vec{m}_i\|^4 + \sum_{j \in 1\text{NN}(i)} J_1 \vec{m}_i \cdot \vec{m}_j + \sum_{j \in 2\text{NN}(i)} J_2 \vec{m}_i \cdot \vec{m}_j \right]. \quad (1)$$

<sup>1</sup>The HL model considers noncollinear magnetism, i.e., magnetic moments are 3D vectors with components  $(m_i^x, m_i^y, m_i^z)$ . However, since spin-orbit coupling is not considered, the absolute orientation of the magnetic moments is not defined with respect to the crystal, only the relative orientations between magnetic moments are relevant.

In the above Hamiltonian,  $A$  and  $B$  are the Landau parameters, controlling longitudinal excitations, i.e., variations of the magnitude of the magnetic moments.  $J_1$  and  $J_2$  are the Heisenberg exchange parameters, controlling transverse excitations, i.e., the relative orientations of magnetic moments. These exchange parameters are defined for a shell of nearest neighbors (NN) of the bcc lattice, namely,  $J_1$  couples first NN (1NN) and  $J_2$  second NN (2NN) atomic sites. Parameters  $A$ ,  $B$ ,  $J_1$ , and  $J_2$  are fitted to the magnetic energy of the three possible collinear ground states of the model, namely, the AF, FM, and B32 structures [15] (see upper row of Fig. 1), as a function of the magnitude  $m_0$  of the magnetic moment. For the FM and B32 magnetic phases, which are unstable, constrained magnetism is used in DFT calculations [13]. Results of these calculations are presented in Fig. 1.

Different values for the lattice parameter  $a_0$  are included in the fit to describe the dependence of the parameters on the distance between atoms. The resulting parameters ( $A$ ,  $B$ ,  $J_1$ ,  $J_2$ ) of the model are presented in Fig. 2(a) as a function of  $a_0$ . Through this procedure, the two  $A$  and  $B$  parameters were almost constant. We therefore set them to a constant value, which yields decreasing exchange couplings  $J_1$  and  $J_2$  with increasing  $a_0$ . The aim of this work being the study of the interplay between magnetic excitations and plasticity, we need to accurately describe the energy of a system which differs from the perfect crystal. To do so, we incorporate a distance dependence in the exchange coupling to consider a system of  $N$  atoms located at positions  $\vec{R}_i$ , and for which the Hamiltonian of Eq. (1) becomes

$$E(\{\vec{m}_i\}, \{\vec{R}_i\}) = \sum_{i=1}^N \left[ A \|\vec{m}_i\|^2 + B \|\vec{m}_i\|^4 + \sum_{j \in \text{NN}(i)} J(r_{ij}) \vec{m}_i \cdot \vec{m}_j \right] \\ \text{with } r_{ij} = \|\vec{R}_i - \vec{R}_j\|, \text{ and } J(r) = \sum_{n=0}^3 j_n r^n, \quad (2)$$

where parameters ( $J_1, J_2$ ) have been replaced by a global function  $J$  of the distance  $r_{ij}$  between the two neighboring atomic sites  $i$  and  $j$ , encapsulating both 1NN and 2NN interactions. A polynomial function of the interatomic distance  $r$  is chosen for  $J$ . This gives the best agreement with respect to DFT data, as a function of both the lattice parameter  $a_0$  and the magnetic moment  $m_0$  [Fig. 2(c)]. However, a range of distances  $r$  is not covered by the fit (between the orange and green shaded regions), in which the variation of the exchange parameter  $J$  with  $r$  is a direct consequence of the polynomial form chosen. A more physical expression can be obtained in the frame of the Ruderman-Kittel-Kasuya-Yosida (RKKY) theory [16], for which indirect exchange coupling is expressed as

$$J_{\text{RKKY}}(r) = J_0 \frac{2kr \cos(2kr) - \sin(2kr)}{r^\alpha}, \quad (3)$$

where  $k$  is the Fermi wave vector,  $J_0$  defines the amplitude of the exchange coupling, and the exponent  $\alpha$  its decay with increasing distance  $r$ . Results obtained from a fit to Eq. (3) are plotted with dashed lines on Fig. 2(c). This theoretical expression of the exchange parameter  $J$  leads to almost the same variations as our empirical polynomial form, with only a very slightly less satisfactory agreement with DFT data. The

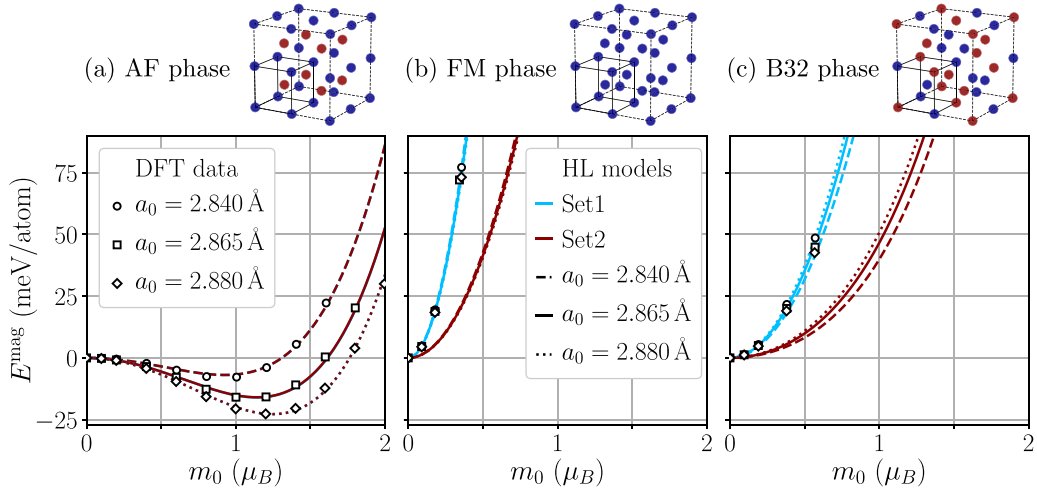


FIG. 1. (a) AF, (b) FM, and (c) B32 magnetic phases included in the fitting procedure of the HL model. Atoms in red (blue) have a positive (negative) magnetic moment. Corresponding magnetic energies  $E^{\text{mag}}$  are shown below as functions of the magnetic moment  $m_0$  at three different lattice parameters  $a_0$ . They are obtained with DFT (symbols) and the HL model (lines). Two different sets of parameters, Set1 (blue) and Set2 (red), are defined for the HL model. These sets lead to the same magnetic energy for the AF phase, but not for the FM and B32 phases.

variations of the exchange parameter obtained by our fitting procedure are therefore fully consistent with RKKY theory, both in the range of distances covered and not covered by DFT data.

Since we aim at the study of finite-temperature magnetic excitations, a good reproduction of the Néel temperature  $T_N$  of bcc Cr must be ensured by the model. As obtained from a direct fit to DFT data, with perfect agreement in the 0-K magnetic properties (see Set1 on Fig. 1), a Néel temperature  $T_N = 1050$  K is predicted by the model, using Monte Carlo simulations (see next section). The model overestimates this temperature, with experiments reporting  $T_N = 311$  K for pristine single crystals [1], and ranging between 300 and 450 K depending on the metallurgical state of the sample (grain size, dislocation density, and whether the material is a powder,

single, or polycrystalline) [2,3]. This overestimation of  $T_N$  is caused by various errors inherent to the DFT calculations, mainly the inability to predict the correct SDW magnetic ground state of bcc Cr (common to all DFT calculations reported in the literature, using various exchange-correlation functionals [10–12]), and the subsequent overestimation of the bulk magnetic moment  $m_0$  (see Table II).

To lower the predicted  $T_N$ , the energies of the two unstable FM and B32 magnetic phases were lowered by a factor  $\frac{1}{4}$  with respect to the reference DFT data. Otherwise, the same DFT database is used, without changing the energy of the ground state AF phase of the model. These new parameters are referred to as Set2, the original parameters being Set1. The resulting fit to the energies of the three collinear phases is also presented in Fig. 1, showing lower energies for the

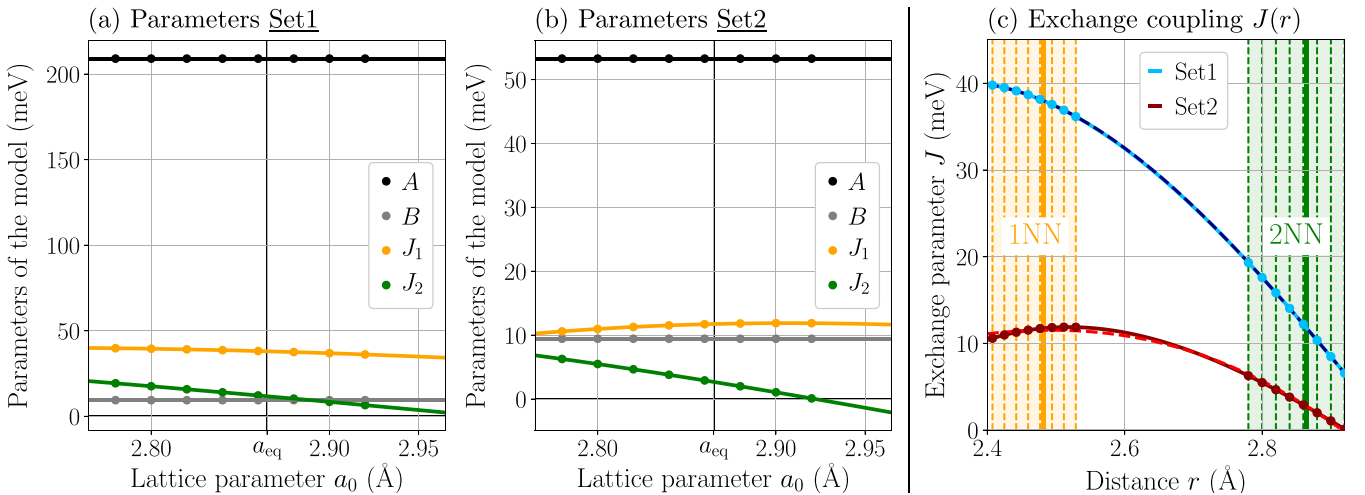


FIG. 2. Variation of the parameters ( $A, B, J_1, J_2$ ) of the HL model with the lattice parameter  $a_0$  for (a) Set1 and (b) Set2. (c) Global exchange coupling  $J$  with respect to the interatomic distance  $r$  using Set1 and Set2 parameters. Results of a fit to Eq. 3 are plotted in dashed colored lines.

TABLE I. Different possible sets of parameters of the HL model [Eq. (2)]. Exchange parameters  $J_1$  and  $J_2$  are given for the equilibrium lattice parameter of the AF phase  $a_0 = 2.865$  Å.

Parameters (meV)	HL (Set1)	HL (Set2)
$A$	209.0	53.0
$B$	9.4	9.4
$J_1$	38.0	11.7
$J_2$	11.8	2.7
$j_0$	-1.75	-1.63
$j_1$	1.94	1.71
$j_2$	-0.67	-0.58
$j_3$	0.07	0.06

two FM and B32 phases than with Set1. This yields a lower predicted  $T_N = 384$  K, in the range of experimental values. However, such an adjustment degrades properties of the model associated with the high-energy FM phase and some magnetic excitation modes, discussed in the next section. We also note different variations of the exchange coupling  $J$  for the two sets [see Fig. 2(c)] across the range between 1NN and 2NN. The values for the two sets of parameters of the model are presented in Table I.

## 2. Validation on 0-K properties

At finite temperature, magnetic fluctuations operate through excitation modes of the spin structure in the form of elementary spin spirals called magnons, defined by their wave vector  $\vec{q}$ . These spirals describe the energetic cost of inducing a disorientation in the magnetic order of the system, while the magnitude of the spins along the propagation of the spiral remains constant. In bulk bcc Cr, these noncollinear structures are known to be highly unstable for any wave vector [12,18]. A direct *ab initio* evaluation of their energy over the whole Brillouin zone would thus be very costly since one needs to account for noncollinear effects in constrained magnetism calculations. A few *ab initio* points were, however, evaluated for small disorientations of the AF order. Such constrained calculations are less costly in the tight-binding (TB) formalism, thus allowing for direct evaluation of the magnon spectrum, i.e., the energy of spirals of wave vector  $\vec{q}$  spanning the entire Brillouin zone. Results of both DFT and TB calculations were obtained using the generalized Bloch's theorem [19], more details about these calculations being presented in Appendix B. The TB results were obtained using the model proposed by Barreateau *et al.* [20] for transition metals, which has proven its ability to describe the magnetic properties of bcc Cr in previous works [12,21,22]. Since the PM phase of bcc Cr above  $T_N$  is mostly characterized by an orientational disorder between magnetic moments [23], an accurate reproduction of these noncollinear spirals is required to have a satisfactory description of magnetic excitations.

Using the HL model, the energy  $E(\vec{q}, m_0)$  of a spin spiral of wave vector  $\vec{q}$  and a constant magnetic moment  $m_0$  has an analytical expression [24]

$$E(\vec{q}, m_0) = A m_0^2 + B m_0^4 + \sum_{k \in \text{1NN}} \sum_{j \in k\text{NN}} J(r_{kj}) m_0^2 \times [1 - e^{i\vec{q} \cdot (\vec{R}_k - \vec{R}_j)}], \quad (4)$$

which corresponds to a sum over the shells of nearest neighbors included in the model. The following expression is obtained considering the two 1NN and 2NN nearest-neighboring shells:

$$E(\vec{q}, m_0) = A m_0^2 + B m_0^4 - 8J_1 m_0^2 \left[ 1 - \cos\left(\frac{a_0 q_x}{2}\right) \times \cos\left(\frac{a_0 q_y}{2}\right) \cos\left(\frac{a_0 q_z}{2}\right) \right] - 2J_2 m_0^2 \times [3 - \cos(a_0 q_x) - \cos(a_0 q_y) - \cos(a_0 q_z)]. \quad (5)$$

The magnon spectrum of bcc Cr over the Brillouin zone is presented in Fig. 3(a) at the equilibrium *ab initio* lattice parameter  $a_0 = 2.865$  Å and magnetic moment  $m_0 = 1.1 \mu_B$ , obtained with Eq. (5) for the HL model, and compared to TB calculations and a few DFT data. The magnon energies are plotted with respect to the AF ground state of the model, i.e.,  $E(\vec{q}, m_0) - E_{\text{AF}}^{\text{mag}}(m_0)$ , to highlight the excitation energy they represent. The special points  $\Gamma$  and  $H$  of the Brillouin zone correspond to the FM and AF magnetic phases, respectively, which are the two extrema of the magnon spectrum according to the three energetic models considered. The magnon density of states (mDOS)  $g(E)$ , shown in Fig. 3(b), is obtained through integration of the spectrum over the entire Brillouin zone.

We report a very satisfactory agreement between the TB spectrum and the few DFT data calculated near the  $H$  point, showing spirals having intermediate energies located between points  $\Gamma$  and  $H$ . These TB results are thus used as a reference to test the validity of the two sets of parameters for the HL model. The spectrum obtained using Set1 (blue) is in good agreement with TB calculations, except near  $P$  where a cusp in the energy of magnons is predicted. Nevertheless, the agreement is particularly satisfactory since the HL model was adjusted on energetics of collinear magnetic phases only. Using the second set of parameters Set2 (red), the model predicts a lower energy for these magnons, with, however, the same variation with  $\vec{q}$  as obtained with Set1. Before moving on to magnetic properties at finite temperatures, we further test the ability of the HL model to reproduce the 0-K magnetic properties of bcc Cr obtained with *ab initio* calculations. The energy of infinite  $\{110\}$  and  $\{112\}$  magnetic faults, obtained by shearing the crystal by a fault vector  $\frac{1}{2}\langle 111 \rangle$  in these two planes, are presented in Table II for DFT and the HL model with the two sets of parameters. We find a very good agreement of the magnetic fault energy  $\gamma$  between *ab initio* calculations and Set1 parameters of the HL model, and a less satisfactory agreement with parameters Set2, a direct consequence of the fitting procedure used to construct it. Indeed, such magnetic faults originate from a ferromagnetic frustration in the two planes located in the direct vicinity of the fault plane, where spins of the same direction are forced to face each other. Since the energy of this highly unstable FM phase has been lowered in the fitting of Set2 parameters, the energy of the fault is lower.



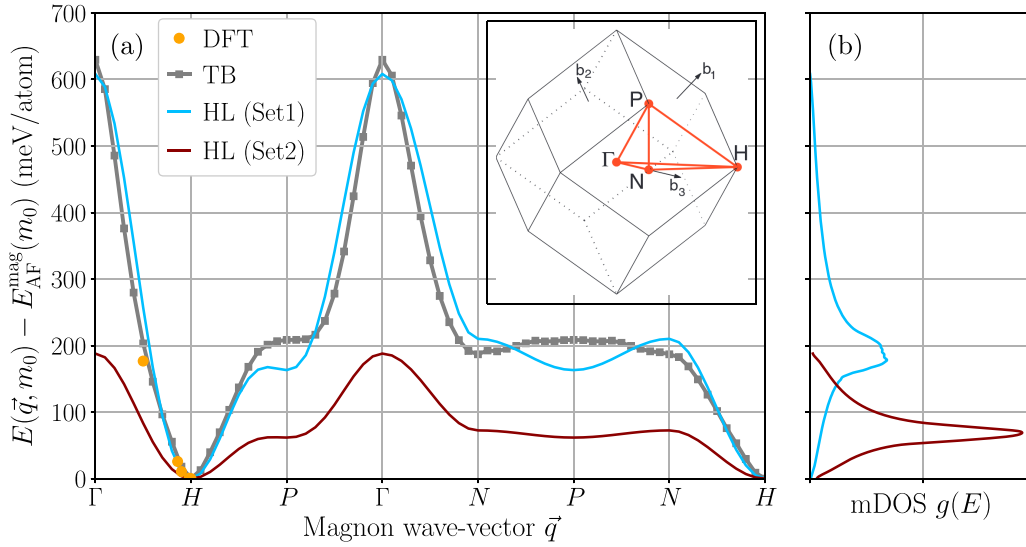


FIG. 3. (a) Magnon spectrum of bcc Cr  $E(\vec{q}, m_0) - E_{\text{AF}}^{\text{mag}}(m_0)$  obtained with constrained *ab initio* DFT calculations (orange dots), the TB model (thick gray lines), and the HL model with Set1 (blue) and Set2 (red) using Eq. (5). Energies are obtained at the equilibrium lattice parameter  $a_0 = 2.865 \text{ \AA}$  and magnetic moment  $m_0 = 1.1 \mu_B$  of the AF phase, along the high-symmetry path  $\Gamma - H - P - \Gamma - N - P - N - \Gamma$  of the Brillouin zone (see inset [17]), with  $\Gamma = (0, 0, 0)$  (FM phase),  $H = (1, -1, 1)$  (AF phase),  $P = (\frac{1}{2}, \frac{1}{2}, \frac{1}{2})$ , and  $N = (0, 0, 1)$ . (b) Magnon density of states (mDOS)  $g(E)$  of the HL model with Set1 and Set2.

### III. FINITE-TEMPERATURE MAGNETIC PROPERTIES

#### A. Monte Carlo simulations

To explore equilibrium magnetic states allowed by finite-temperature excitations, Monte Carlo simulations are performed on a system of  $N$  atoms, arranged on rigid lattice sites (which can differ from the perfect bulk structure<sup>2</sup>) with magnetic moments  $\vec{m}_{i \in [1, N]}$  and whose energy is described by the

<sup>2</sup>Since magnetic degrees of freedom are much faster than atomic vibrations, such an adiabatic approximation appears legitimate. To treat both atomic and magnetic degrees of freedom, one would need an interatomic potential on top of which is plugged, for instance, an effective magnetic interaction model such as developed here, which is not the scope of this study.

TABLE II. Computed properties of the HL model, compared to collinear (“Col.”) and noncollinear (“NC”) DFT calculations and experimental data: bulk magnetic moment  $m_0$  of the AF phase, energy of the NM and SDW (of period  $20a_0$ ) phases with respect to the AF phase, energy  $\gamma$  of the magnetic fault in {110} and {112} planes, and Néel temperature  $T_N$ . All quantities have been calculated for a lattice parameter  $a_0 = 2.865 \text{ \AA}$ . The experimental magnetic moment is given for the peak magnitude of the SDW.

	DFT		HL model		Expt.
	Col.	NC	Set1	Set2	
$m_0 (\mu_B)$	1.10	1.10	1.14	1.14	0.62 [25]
$\Delta E_{\text{NM}} (\text{meV/atom})$	12.5	12.5	12.5	12.5	
$\Delta E_{\text{SDW}} (\text{meV/atom})$	10.4	10.4	8.6	4.8	
$\gamma_{\{110\}} (\text{meV/\AA}^2)$	16.2	16.2	15.1	8.7	
$\gamma_{\{112\}} (\text{meV/\AA}^2)$	16.1	16.4	15.1	8.7	
$T_N (\text{K})$			1 050	384	311 [1]

HL model of Eq. (2). Periodic boundary conditions are used in all directions. The system is equilibrated at the simulated temperature  $T$  through a number of Metropolis Monte Carlo steps consisting in a random change of the three Cartesian components of one of the  $N$  spins. At each step, the change  $\delta E$  in the energy of the system is evaluated, and the transition is then accepted or rejected based on the probability distribution:

$$p(\delta E) = \begin{cases} 1, & \text{if } \delta E \leq 0 \\ \exp\left[-\frac{\delta E}{\eta(T)}\right], & \text{if } \delta E > 0. \end{cases} \quad (6)$$

This probability depends on the statistics  $\eta(T)$  used in the simulation, which within classical statistics is the Boltzmann distribution given by  $\eta(T) = k_B T$ .

However, since the energy of magnetic excitations described by the model is continuous, this allows for fluctuations in the magnitude and orientation of the spins even at low temperatures where quantum effects should prevent it, yielding nonphysical thermodynamic properties [26]. Considering discrete energy levels, in the form of magnons, these continuous thermal excitations are not allowed at low temperature. This quantification of the energy levels can be accounted for, using the method described in Refs. [26,27], by the approximate quantum statistics:

$$\eta_Q(T) = \int_0^\infty \frac{E}{\exp\left(\frac{E}{k_B T}\right) - 1} g(E, T) dE, \quad (7)$$

where  $E$  is the magnon energy, and  $g(E, T)$  is the mDOS at temperature  $T$  and energy  $E$ . The key to construct such quantum statistics is thus the knowledge of the temperature-dependent mDOS,  $g(E, T)$ , which is derived from the 0-K results presented in Fig. 3(b) following the method of Woo *et al.* [27]. Details about the construction of this finite-temperature mDOS and results of this quantum statistics are given in Appendix A. In the following, magnetic excitations

will be studied using the approximate quantum statistics of Eq. (7) at low temperature, i.e., below  $T_N$ , and classical Boltzmann statistics above  $T_N$ .

The Monte Carlo sampling with temperature  $T$  then allows to access thermodynamic equilibrium properties of the system through ensemble average of the magnetic internal energy  $E^{\text{mag}}$  at  $T$ . The magnetic free energy  $F^{\text{mag}}$  of the system is evaluated through its thermodynamic integration, however requiring to set a reference at which its value is known. This reference is set at a temperature  $T_{\text{ref}}$ , whose choice depends on the system. For this purpose, it is convenient to work with the inverse temperature  $\beta = 1/k_B T$  to express thermodynamic quantities of interest, resulting in

$$\beta F^{\text{mag}}(\beta) - \beta_{\text{ref}} F^{\text{mag}}(\beta_{\text{ref}}) = \int_{\beta'=\beta_{\text{ref}}}^{\beta} E^{\text{mag}}(\beta') d\beta'. \quad (8)$$

Now considering a system containing a defect, like a magnetic fault or a dislocation dipole, the excess magnetic internal  $\Delta E^{\text{mag}}$  and free  $\Delta F^{\text{mag}}$  energies are

$$\begin{aligned} \Delta E^{\text{mag}}(\beta) &= E_{\text{defect}}^{\text{mag}}(\beta) - E_{\text{bulk}}^{\text{mag}}(\beta), \\ \Delta F^{\text{mag}}(\beta) &= F_{\text{defect}}^{\text{mag}}(\beta) - F_{\text{bulk}}^{\text{mag}}(\beta), \end{aligned} \quad (9)$$

where  $E_{\text{defect}}^{\text{mag}}$  and  $E_{\text{bulk}}^{\text{mag}}$  refer to the energy of the simulation cell containing the defect and the perfect crystal, respectively. Applying Eq. (8) to these excess magnetic energies, we obtain

$$\beta \Delta F^{\text{mag}}(\beta) - \beta_{\text{ref}} \Delta F^{\text{mag}}(\beta_{\text{ref}}) = \int_{\beta'=\beta_{\text{ref}}}^{\beta} \Delta E^{\text{mag}}(\beta') d\beta'. \quad (10)$$

Two different defects are studied in bcc Cr using this method: magnetic faults caused by a  $\frac{1}{2}\langle 111 \rangle$  shear, and the magnetic contribution to the core energy of  $\frac{1}{2}\langle 111 \rangle$  screw dislocations. In both cases, we assume that  $\Delta F^{\text{mag}}(\beta_{\text{ref}}) = 0$  setting the reference temperature above the Néel temperature  $T_{\text{ref}} = 5T_N/4$ , where the system is in the disordered PM phase. We then checked that the excess magnetic energy contained in a faulted simulation cell is zero at this temperature, i.e., the system has the same magnetic energy whether a defect is present or not. In this case, the magnetic free energy  $\Delta F^{\text{mag}}$  of the defect can be expressed as

$$\Delta F^{\text{mag}}(\beta) = \frac{1}{\beta} \int_{\beta'=\beta_{\text{ref}}}^{\beta} \Delta E^{\text{mag}}(\beta') d\beta'. \quad (11)$$

All simulation cells have periodic boundary conditions in all directions, and contain approximately 14 000 atoms, allowing for magnetic fluctuations to occur without boundary effects. The system is equilibrated using  $10^8$  Metropolis Monte Carlo steps at each temperature, ensuring convergence of thermodynamic properties. For 0-K calculations, magnetic structures are relaxed using an infinite quench where only events leading to a decrease of the energy are accepted.

### B. Finite-temperature bulk magnetic properties

A first step to test the presented model is the evaluation of the Néel temperature  $T_N$ , and thus the properties of the PM phase where magnetic long-range order (MLRO) vanishes. A measure of MLRO is obtained through an order parameter  $O$  defined as the sum of the average magnetizations over the two

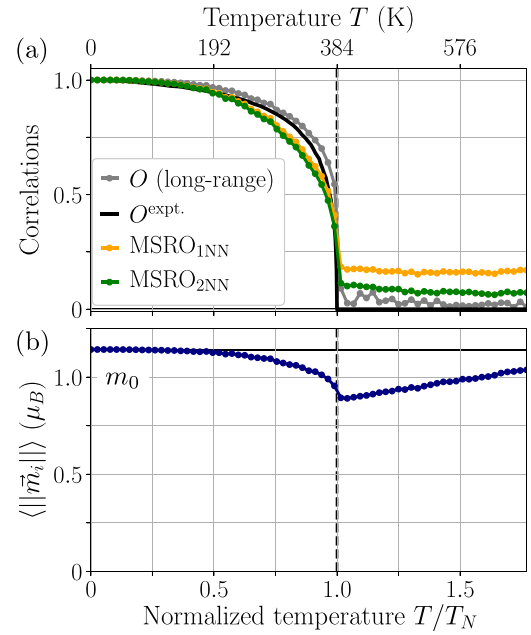


FIG. 4. (a) Measure of magnetic long-range order through the order parameter of Eq. (12) (gray) compared to experimental data from Ref. [1] (black), and the average MSRO between first (orange) and second (green) nearest neighbors, all as a function of temperature. (b) Average magnetic moment  $\langle ||\vec{m}_i|| \rangle$  as a function of temperature. Results are obtained using Set2 parameters for the HL model. The absolute temperature scale above the plots is the theoretical one.

sublattices  $S_1$  and  $S_2$  of the AF order, i.e., with spins  $\uparrow$  and  $\downarrow$ , respectively:

$$O = \frac{1}{m_0} \left[ \frac{\| \sum_{i \in S_1} \vec{m}_i \|}{N/2} + \frac{\| \sum_{j \in S_2} \vec{m}_j \|}{N/2} \right], \quad (12)$$

with  $m_0$  the 0-K bulk magnetic moment, and  $N$  the number of atoms contained in the simulation cell. When the system is in its AF ground state, the order parameter is equal to 1, with all magnetic moments of magnitude  $m_0$  and opposite signs on each sublattice. The evolution of the order parameter with temperature using Set2 parameters and the quantum statistics is presented in Fig. 4(a) (gray), and compared with experimental data [1] (black), with a predicted Néel temperature  $T_N$  of 384 K. As a reference, the experimental  $T_N$  of perfect single crystal of bcc Cr is 311 K [1]. We note that quantization of magnetic excitations yields a slow decrease close to 0 K, in good agreement with experiments, with a drop at  $T_N$ . To fully qualify the magnetic properties of the PM phase, another important quantity is the remaining magnetic short-range order (MSRO), which is measured as the average correlations between magnetic moments of neighboring atoms:

$$\begin{aligned} \text{MSRO}_{n\text{NN}} &= \frac{1}{m_0^2} \langle \vec{m}_i \cdot \vec{m}_j \rangle \\ &= \frac{1}{m_0^2} \left[ \frac{1}{N} \sum_{i=1}^N \frac{1}{Z_n} \sum_{j \in n\text{NN}(i)} \vec{m}_i \cdot \vec{m}_j \right], \end{aligned} \quad (13)$$

where  $n\text{NN}$  is the  $n$ th shell of nearest neighbors containing  $Z_n$  sites. The correlation between two magnetic moments is

calculated as the scalar product between them. The temperature variation of the average MSRO between first-nearest (1NN, in orange) and second-nearest (2NN, in green) neighbors are presented in Fig. 4(a). Remaining MSRO has been observed experimentally up to approximately 11 bcc unit cells at 700 K (i.e.,  $2.25 \times T_N$ ) by Grier *et al.* [28] using neutron diffraction. Other references, using similar neutron scattering experiments, showed persistence of magnetic order in the PM phase up to lower temperatures of approximately 500 K (i.e.,  $1.6 \times T_N$ ) [25,29]. Results presented in Fig. 4(a) show the disappearance of long-range order and a remaining MSRO above  $T_N$ , in qualitative agreement with experiments, with stronger correlations between 1NN than 2NN neighbors.

Neutron diffraction [28,30,31] and x-ray photoelectron spectroscopy [23] experiments also demonstrated the persistence of atomic magnetic moment above  $T_N$  in this disordered PM phase of Cr. To study this effect, the variation of the average magnetic moment with temperature is presented in Fig. 4(b), which shows a slow decrease from its value  $m_0$  at 0 K up to  $T_N$ , at which it starts increasing again. This effect is caused by the decreasing MSRO, which yields magnetic frustrations, partially resolved through a reduction in their magnetic moments. Above  $T_N$ , thermal energy allows higher magnitude of the magnetic moments, which gradually increase. This demonstrates that the magnetic disorder in the PM phase is rather orientational, and not associated to a drop in the magnetic moment.

All results obtained at finite temperature presented here were obtained using Set2 parameters. Qualitatively similar results were, however, obtained using Set1 parameters of the model, with a shifted temperature scale given the higher Néel temperature  $T_N = 1050$  K predicted using these parameters. Both Set1 and Set2 parameters are intended for different properties: Set1 gives better 0-K energies with respect to *ab initio* calculations, while Set2 gives a good reproduction of the experimental value of  $T_N$ , with less satisfactory 0-K properties.

#### IV. MAGNETISM AND PLASTICITY OF CHROMIUM AT FINITE TEMPERATURE

We now study the temperature evolution of the magnetic frustrations generated by  $\frac{1}{2}\langle 111 \rangle$  shear up to  $T_N$ , both looking at magnetic faults and dislocation dipoles. A previous work [5] based on results obtained at 0 K concluded that these faults are the only significant impact of magnetism on the plasticity of Cr, their energy being the main controlling parameter. All presented results are obtained using Set2 parameters of the HL model unless otherwise specified.

##### A. Infinite magnetic faults

The magnetic energy of such infinite magnetic fault is evaluated as the excess energy of a crystal sheared in a plane by a  $\frac{1}{2}\langle 111 \rangle$  vector with respect to the perfect crystal. The simulation cell has periodicity vectors  $X = 8 \times [\bar{1}2\bar{1}]$ ,  $Y = 11 \times [111]$ , and  $Z = 13 \times [\bar{1}01]$  for the perfect crystal, and the  $(\bar{1}01)$  and  $(\bar{1}2\bar{1})$  magnetic faults are modeled by adding a  $\frac{1}{2}[111]$  component respectively to the  $Z$  and  $X$  periodicity vectors. The internal and free energies of the obtained magnetic faults are presented in Fig. 5 as a function of temperature.

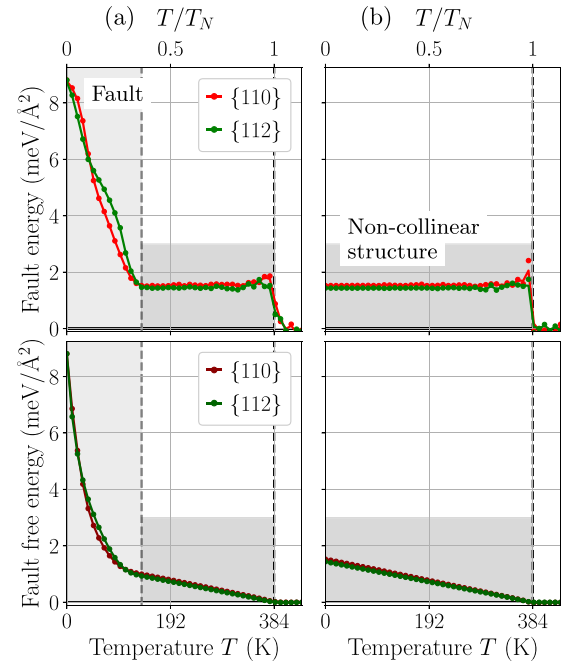


FIG. 5. Magnetic fault energy  $\Delta E^{\text{mag}}$  (first row) and free energy  $\Delta F^{\text{mag}}$  (second row) of the two infinite {110} (red) and {112} (green) magnetic faults as a function of temperature upon (a) heating and (b) cooling the system.

The heat cycle is shown in Fig. 5(a), where temperature is increased from 0 K with all magnetic moments initialized to the AF ground state in all three Cartesian directions, i.e.,  $m_i^x = m_i^y = m_i^z = m_0/\sqrt{3}$ , where  $m_0$  is the 0-K bulk magnetic moment. Similarly, the cooling cycle is presented in Fig. 5(b), where the system is initialized in its disordered PM phase at temperature  $5T_N/4$ , before being cooled down to 0 K. The same behavior is observed for both {110} and {112} faults.

Upon heating the system, the energy of the magnetic fault [upper panel in Fig. 5(a)] starts at the 0-K value for the two {110} (red) and {112} (green) planes, before decreasing up to approximately 140 K. Above, the excess magnetic energy in the simulation cell stays constant, before vanishing at  $T_N$ , where the disappearance of long-range magnetic order does not allow such fault to exist anymore. The situation is different when the system is cooled from temperatures above  $T_N$ , showing a constant magnetic excess energy as soon as magnetic order is recovered, all the way down to 0 K. The excess magnetic energy is the same as found upon heating the same system in the temperature range between 140 K (i.e.,  $\approx T_N/3$ ) and  $T_N$ . The free energy of the magnetic faults in {110} and {112} planes is presented in the lower panels of Fig. 5. When the system is heated from 0 K, we report a steep decrease of the excess magnetic energy up to approximately 140 K, and a linear decrease above. Upon cooling the system, the magnetic free energies show a linear increase with  $T$  as soon as magnetic order is retrieved at  $T_N$ , matching the profiles found above 140 K upon heating.

Following the two thermal cycles presented in Fig. 5, the magnetic structure of the system takes two different configurations, which are presented in Fig. 6. Results are only shown for the {110} structure, however, identical structures are found



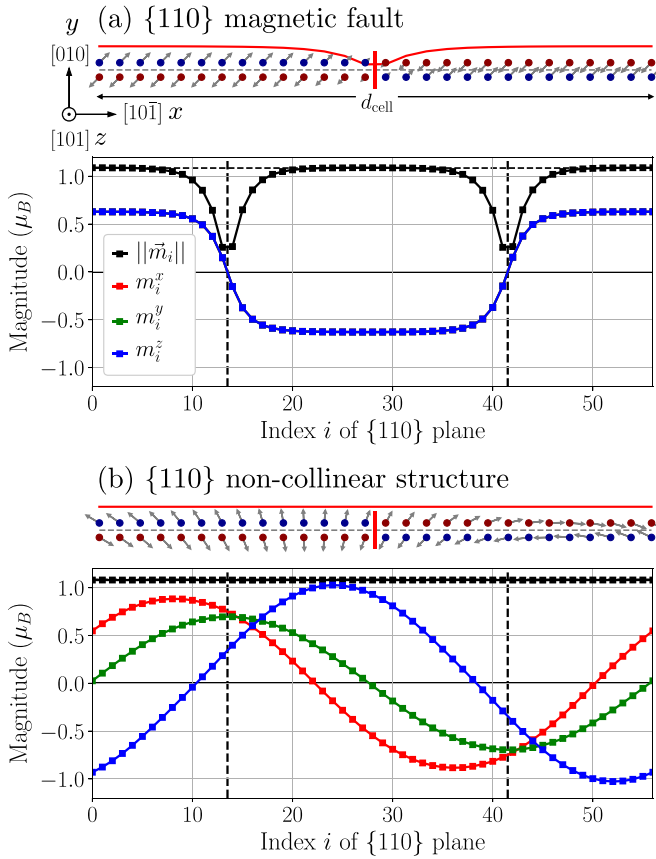


FIG. 6. Structure of the  $\{110\}$  (a) magnetic fault, and (b) non-collinear structure obtained at 0 K upon cooling, with the profiles of the three Cartesian components of the magnetic moments  $\vec{m}_i$  along the  $[10\bar{1}]$  direction normal to the fault plane. The fault planes are indicated by dashed vertical black lines. Relaxation using noncollinear *ab initio* calculations leads to identical structures.

for a  $\{112\}$  fault plane. We first consider the collinear structure (upper row in Fig. 6), which corresponds to the configuration of the system below 140 K upon heating. The variation of the magnetic moments  $\vec{m}_i$  along the direction orthogonal to the fault plane shows that all three Cartesian components of the spins decrease down to zero in the vicinity of the fault plane (indicated by black vertical dashed lines), with  $m_i^x = m_i^y = m_i^z$ . This structure is identical to the one obtained at 0 K with *ab initio* calculations [5]. The fault is thus confined in the vicinity of the sheared plane, with a similar structure upon heating up to 140 K.

Now considering the magnetic structure found between 140 K and  $T_N$  upon heating, or below  $T_N$  upon cooling, it is noncollinear, with a structure similar to a spin spiral (Fig. 6, lower panel). These spirals are defined by a relative disorientation of the magnetic moments, keeping a constant magnitude along their propagation direction. In this configuration, the perturbation spreads over the entire simulation cell, instead of being localized in the fault plane. The periodicity of the spiral is dictated by the length of the simulation cell in the direction perpendicular to the initial fault plane  $d_{\text{cell}}$ . With the inclusion of noncollinear magnetism, another possibility to resolve the magnetic frustration is indeed to induce

a disorientation of magnetic moments, keeping a constant magnitude, in the direction orthogonal to the fault plane, keeping a local AF magnetic order in each stacked plane. The energy cost associated with such disorientational perturbation is less than a local reduction of the amplitude of the magnetic moments in the vicinity of the fault plane, as can be noted from Fig. 5. These spirals thus correspond to the true magnetic ground state of the faulted crystal, with lower magnetic energies than collinear faults.

Similar to a propagating wave, the nodes of the spiral in the three Cartesian components of the magnetic moments  $\vec{m}_i$  can be located anywhere along its propagation direction since they are not bounded to any topological defect. Such a magnetic structure with nonzero excess energy with respect to the AF ground state is thus stabilized upon cooling the system due to the constraint imposed by the periodicity vectors of the simulation cell, which are sheared by the same amount as the fault plane, thus forcing two spins with the same sign to face each other. Looking at this noncollinear structure, it is clear that the perturbation is not localized in a defined plane and does not correspond to a fault. It is better described as a spiral, identical to a magnon excitation located between special points  $H$  and  $\Gamma$  of the Brillouin zone on the spectrum of Fig. 3. We then checked with *ab initio* calculations, including noncollinear magnetism and spin-orbit coupling (see details in Appendix B), that these spiral structures predicted by the HL model are indeed stable. The relaxed magnetic structures are found identical to the predictions of the HL model, as for instance presented in Fig. 6 for the  $\{110\}$  plane. The orientation of the *ab initio* magnetic moments is given with respect to the given crystal directions. On the other hand, since spin-orbit coupling is not accounted for by the HL model, the choice for the orientation of the magnetic moments obtained from the model are therefore arbitrary with respect to the lattice, which we chose to match the *ab initio* results for representation. To highlight that these noncollinear structures do indeed not correspond to a fault, we study their energies at 0 K as a function of the distance  $d_{\text{cell}}$ , and compare the results with the case of the collinear magnetic fault. The magnetic energies are presented in Fig. 7 in both  $\{110\}$  and  $\{112\}$  planes, using the HL model, and compared to the results of *ab initio* calculations. As opposed to the magnetic fault, whose energy  $\gamma_{\text{fault}}$  converges to a constant nonzero value, the surface energy of the noncollinear structure tends to zero for an infinite separation distance  $d_{\text{cell}}$  between periodic images of the fault, in both  $\{110\}$  and  $\{112\}$  planes. The slope of this decreasing excess energy is the same in both planes, with a very good agreement between DFT and the HL model for Set1 parameters, 237 and 224 meV/Å, respectively, with DFT predicting a small offset for infinite distances. Description of this noncollinear structure as a fault thus does not hold since convergence of its energy cannot be achieved by increasing the length  $d_{\text{cell}}$ . As detailed above, these noncollinear structures are similar to spin spirals. Thus, when the length  $d_{\text{cell}}$  of the simulation cell increases, the disorientation imposed between each atomic layer by the faulted periodicity vectors decreases, tending to zero for an infinite length, where the AF order is retrieved. The excess energy of this structure thus falls to zero, a behavior confirmed by *ab initio* calculations.

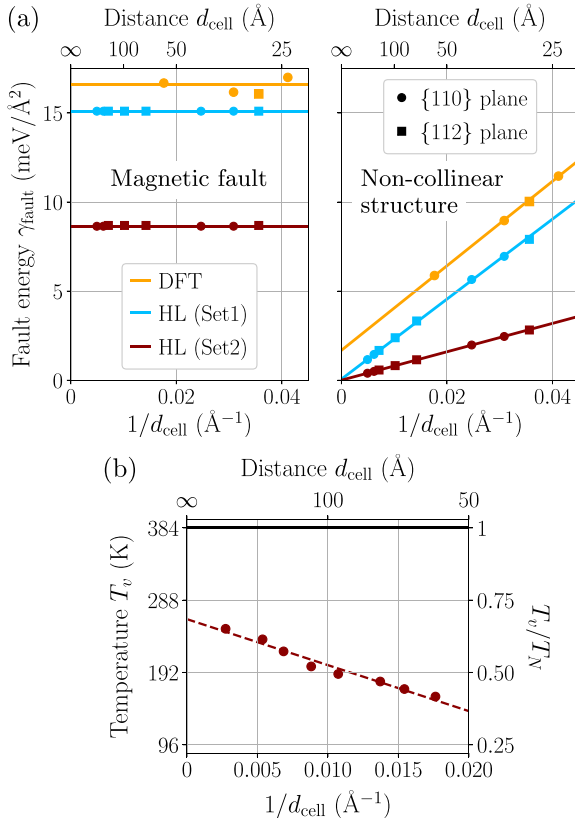


FIG. 7. (a) Energy  $\gamma_{\text{fault}}$  at 0 K of the magnetic fault (left), and the noncollinear structure (right) as a function of the separation distance  $d_{\text{cell}}$  between {110} (circles) and {112} (squares) fault planes obtained with *ab initio* calculations (orange) and the HL model with Set1 (blue) and Set2 (red) parameters. (b) Temperature  $T_v$  at which the {110} magnetic fault vanishes as a function of the separation distance  $d_{\text{cell}}$  obtained with Set2 parameters of the HL model.

Since the excess magnetic energy of the noncollinear structure decreases with the length of the simulation cell, the temperature at which the collinear magnetic fault destabilizes in favor of this noncollinear perturbation also depends on the size of the simulated volume. The dependence of this vanishing temperature  $T_v$  as a function of the distance  $d_{\text{cell}}$  is studied using various simulation cells with axis  $x \parallel [\bar{1}2\bar{1}]$ ,  $y \parallel [111]$ , and  $z \parallel [\bar{1}01]$ , keeping a constant simulated volume, but varying the length  $d_{\text{cell}}$  in the  $z$  direction, with a rigid  $\frac{1}{2}[111]$  shearing. All magnetic moments are initialized at their AF ground-state configuration, and the systems are then heated starting from 0 K. The temperature  $T_v$  at which the 0-K magnetic fault vanishes in favor of the noncollinear structure, presented in in Fig. 7(b), shows an increase up to approximately  $2T_N/3$  in the limit of an infinitely long simulation cell. The magnetic faults therefore become unstable well below the Néel temperature, with relaxation to a noncollinear structure.

### B. Dislocation dipole

We now study the magnetic structure of a crystal sheared by a  $\frac{1}{2}\langle 111 \rangle$  screw dislocation dipole as a function of temperature. We showed in the previous section that the shearing

of an infinite crystal by  $\frac{1}{2}\langle 111 \rangle$  could be accommodated by a noncollinear magnetic structure differing from a fault, which we now intend to extend to the case of a magnetic frustration caused by dislocations.

The simulation cell is constructed in a similar way to supercells used for *ab initio* calculations on  $\frac{1}{2}\langle 111 \rangle$  screw dislocations in bcc metals [32], with periodicity vectors  $\vec{p}_1 = 21/2[\bar{1}2\bar{1}] - 39/2[\bar{1}01]$ ,  $\vec{p}_2 = 21/2[\bar{1}2\bar{1}] + 39/2[\bar{1}01]$ , and  $\vec{p}_3 = 6 \times \frac{1}{2}[111]$ , containing a total of 14 742 atoms. The dislocation dipole is introduced in a quadrupolar arrangement using anisotropic elasticity theory, with the magnetic fault laying in the (101) plane, with a distance  $d = 74$  Å between the two dislocations. The cell is  $6b$  high, which is sufficiently large to allow for magnetic fluctuations in each direction without periodic boundary effects. The structure of the magnetic fault bounded by the two  $\frac{1}{2}[111]$  screw dislocations of the dipole is presented in Fig. 8 at three different temperatures, recorded upon heating the system starting from 0 K and initializing all magnetic moments to their AF configurations, with  $m_i^x = m_i^y = m_i^z = m_0/\sqrt{3}$ .

The collinear magnetic fault found at 0 K, contained in the (101) plane [Fig. 8(a)], has an identical structure to the infinite fault shown in the previous section, with a reduction of the magnetic moments in the vicinity of the fault plane in the region bounded by the two  $\frac{1}{2}[111]$  dislocations to accommodate the magnetic frustration. We also note that this structure is similar to the fault obtained using *ab initio* calculations at 0 K [5]. As the temperature is increased up to 150 K [see Figs. 8(b) and 8(c)], the region where each of the three Cartesian components of the magnetic moments cancels starts to fluctuate in space. Through magnetic excitations, the fault caused by the dislocations is allowed to take a noncollinear structure where the frustration is partially resolved by inducing a disorientation of the spins in the region bounded by the two  $\frac{1}{2}[111]$  screw dislocations, similar to the case of the infinite fault. The magnitude of the spins is constant almost over the whole simulation cell, except in the direct vicinity of the dislocation cores where the strong lattice distortion causes a local reduction of the magnetic moments. Even if there is a signature of a magnetic fault, since the perturbation remains bounded by the two dislocations, its structure differs from the infinite case, which is here an orientational perturbation rather than a drop in the magnetic moments. At higher temperatures, the progressive spreading of this noncollinear perturbation leads to the vanishing of the magnetic fault.

The noncollinear magnetic structure obtained upon cooling the system from the high-temperature PM phase above  $T_N$  down to 0 K is presented in Fig. 9. Profiles of the magnetic moments along the thick yellow dashed lines reveal the magnetic structure in directions orthogonal and contained in the plane defined by the two  $\frac{1}{2}[111]$  screw dislocations of the dipole, showing a similar but more complex structure as obtained in the infinite case of the previous section. Indeed, the three components of the spins show a modulation differing from a sinusoidal wave in the direction orthogonal to the plane defined by the two dislocations, especially for the  $m_i^z$  component as shown in the upper panel of Fig. 9(c). Another important feature of this structure, which is better visualized on the spin maps of Figs. 9(a) and 9(b), is that

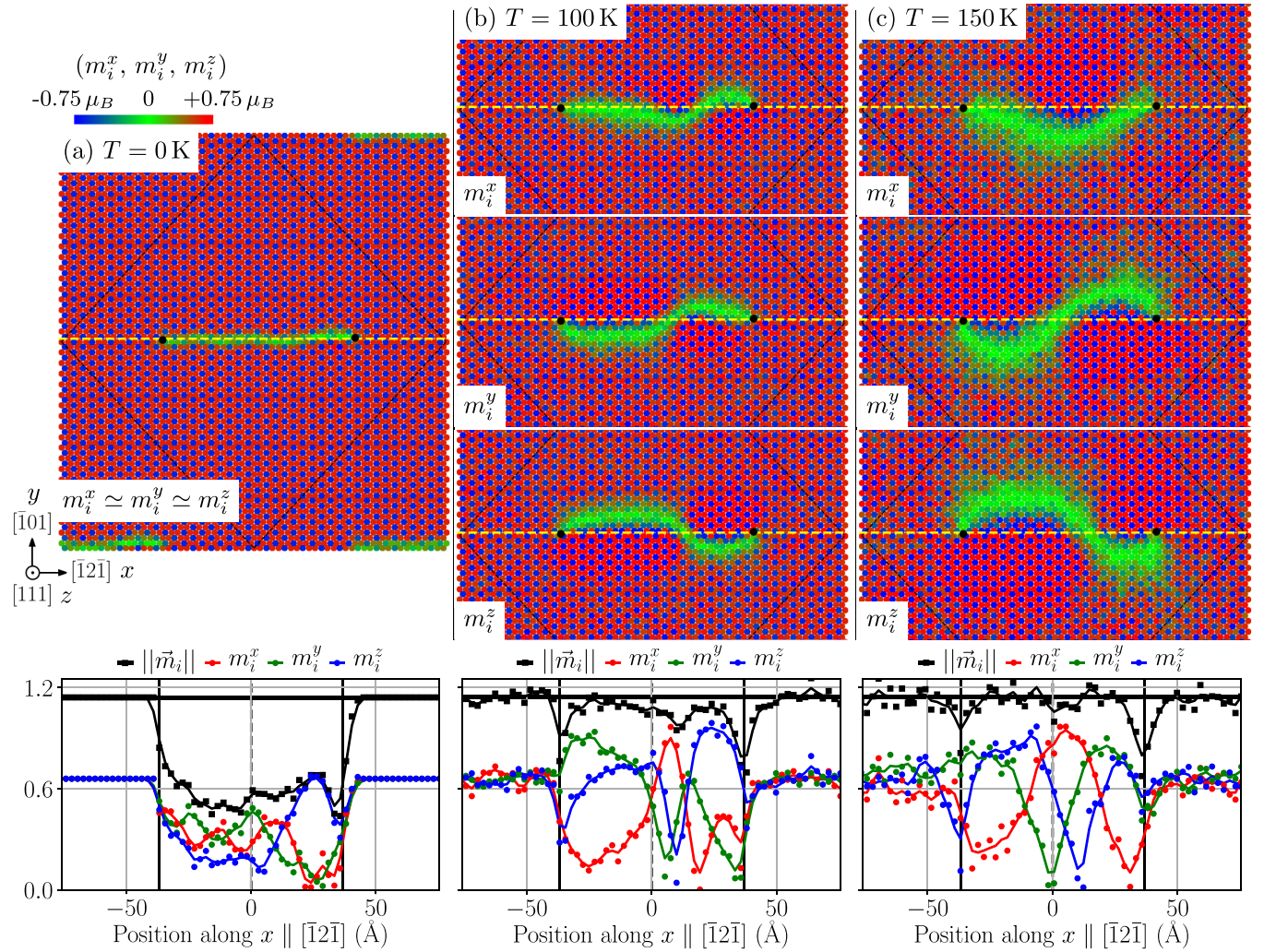


FIG. 8. Evolution of the magnetic structure bounded by two  $\frac{1}{2}[111]$  screw dislocations (black dots) upon heating from the 0-K collinear configuration in (a) to (b) 100 K ( $\simeq T_N/4$ ) and (c) 150 K ( $\simeq 2T_N/5$ ). The colors correspond to the projections  $m_i^x$ ,  $m_i^y$ , and  $m_i^z$  of the magnetic moments along the  $\bar{x}$ ,  $\bar{y}$ , and  $\bar{z}$  axis, respectively, according to the legend shown in (a). Profiles of the magnetic moments along the  $x$  yellow dashed lines in each map are plotted in the lower panel. Configurations are presented in the plane orthogonal to the direction  $Z$  of the dislocation line at  $z = h/2$ , with  $h$  the height of the simulation cell. The magnetic structure of the system is, however, identical in each  $1b$  slice along  $Z$ .

this noncollinear structure is not confined in the vicinity of the plane defined by the relative positions of the two dislocations, contrary to the low-temperature magnetic fault, but instead spreads over the entire simulation cell. We will show in the next section that this noncollinear magnetic structure surrounding the  $\frac{1}{2}\langle 111 \rangle$  dislocation dipole is more stable than the magnetic fault bounded by the two dislocations.

### C. Magnetic contributions to dislocation energy

We now study the temperature evolution of the magnetic contribution to the excess energy of  $\frac{1}{2}\langle 111 \rangle$  screw dislocations. The total magnetic energy of a simulation cell containing a dislocation dipole is partitioned as

$$E_{\text{tot}}^{\text{mag}} = E_{\text{bulk}}^{\text{mag}} + E_{\text{fault}}^{\text{mag}} + 2E_{\text{core}}^{\text{mag}} + E_{\text{elas}}^{\text{mag}}, \quad (14)$$

where we will show in the following that the magnetic elastic contribution  $E_{\text{elas}}^{\text{mag}}$  is negligible when evaluating the excess magnetic energy of a dislocation dipole. *A priori*, this assumption

appears legitimate given the magnetic contribution to the elastic moduli  $C'$  and  $C_{44}$  (to which the elastic energy of a  $\frac{1}{2}\langle 111 \rangle$  screw dislocation dipole is proportional) predicted by the HL model are  $-4\%$  ( $-8.9$  GPa) and  $22\%$  (21.3 GPa), respectively. The magnetic fault energy is proportional to its surface  $d \times h$  with  $h$  the height of the simulation cell in the  $\langle 111 \rangle$  direction and  $d$  the distance between the two dislocations of the dipole,  $E_{\text{fault}}^{\text{mag}} = d h \gamma_{\text{fault}}^{\text{mag}}$ . Neglecting the contribution to the elastic energy, the total excess magnetic energy contained in the simulation cell at a temperature  $T$  is then given by

$$\begin{aligned} \Delta E^{\text{mag}}(d, T) &= E_{\text{tot}}^{\text{mag}} - E_{\text{bulk}}^{\text{mag}} \\ &= d h \times \gamma_{\text{fault}}^{\text{mag}}(T) + 2E_{\text{core}}^{\text{mag}}(T). \end{aligned} \quad (15)$$

The magnetic energy of the bulk  $E_{\text{bulk}}^{\text{mag}}$  is evaluated in the same simulation cell as presented in Figs. 8 and 9, before introducing the  $\frac{1}{2}\langle 111 \rangle$  screw dislocation dipole. The above partition of the excess magnetic energy  $\Delta E^{\text{mag}}$  is expressed as a linear



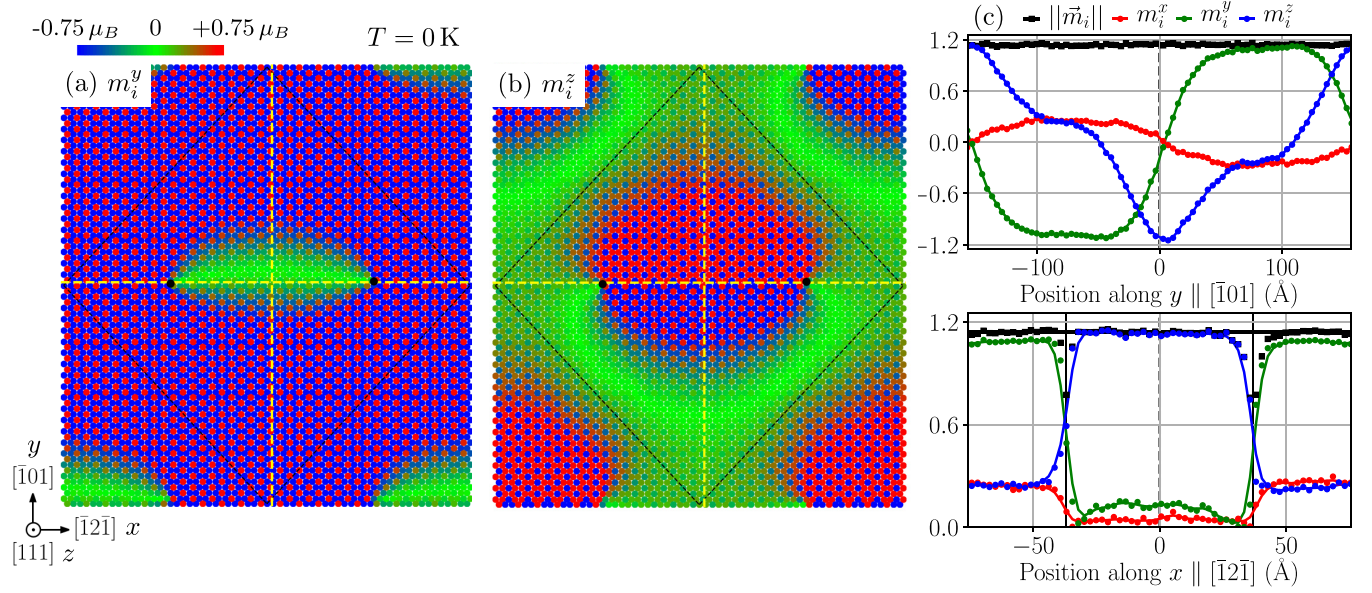


FIG. 9. Noncollinear structure bounded by two  $\frac{1}{2}[111]$  screw dislocations (black dots) projected along (a)  $\bar{y}$  and (b)  $\bar{z}$ . (c) Profile of the magnetic moments along the  $x$  and  $y$  yellow dashed lines in (a) and (b). The structure is presented at 0 K, obtained upon cooling the system starting from initially random spins in the PM phase.

function of the distance  $d$  between the two dislocations of the dipole, with a slope corresponding to the surface energy of the fault  $\gamma_{\text{fault}}$ . Taking advantage of Eq. (15) using the same simulation cell as in the previous section, the distance  $d$  is varied to reduce the range of the magnetic fault, allowing for the evaluation of the magnetic energy of the system as a function of both  $d$  and the temperature  $T$ . All dislocated simulation cells are constructed using anisotropic elasticity theory, similar to the previous calculations. However, the dislocation dipole is no longer quadrupolar as the distance  $d$  is varied. The setup is otherwise identical, with the dipole laying in the  $(\bar{1}01)$  plane in the same simulation cell, thus with the same number of atoms. The variation of the excess energy  $\Delta E^{\text{mag}}$  as a function of the distance  $d$  at various temperatures is presented in Fig. 10, upon heating in (a), and cooling in (b). A fit of the energies  $\Delta E^{\text{mag}}$  of these different systems to Eq. (15) at a given temperature  $T$  then allows to simultaneously extract the magnetic contribution to the core energy of the dislocations  $E_{\text{core}}^{\text{mag}}$ , and the magnetic fault energy  $\gamma_{\text{fault}}$  at this temperature  $T$ . The linear fits are very satisfactory above a certain distance marked by a vertical black dashed line, below which the excess magnetic energy does not behave linearly, probably due to finite-size effects for short separation distances. The magnetic energies of interest are therefore obtained from fitting to the excess energies obtained for larger distances  $d$ . This demonstrates the validity of the proposed decomposition of the total magnetic energy of the system [Eq. (14)], and that the elastic contribution to the magnetic energy of the dipole is indeed negligible, at least up to temperatures close to  $T_N$  where fluctuations deteriorate this linear variation. This allows for a separate definition of the magnetic contributions of the fault and dislocation cores. This confirms that the magnetic contribution to the elastic energy can be neglected as it would have lead to a contribution varying in  $\ln(d)$ , thus deviating from the observed linear variation.

The slope and value for  $d = 0$  obtained from Fig. 10 gives the energy  $\gamma_{\text{fault}}$  of the magnetic fault, and the magnetic core energy  $E_{\text{core}}^{\text{mag}}$ , respectively, which are presented in Fig. 11 as a function of  $T$ , upon both heating and cooling the system. The

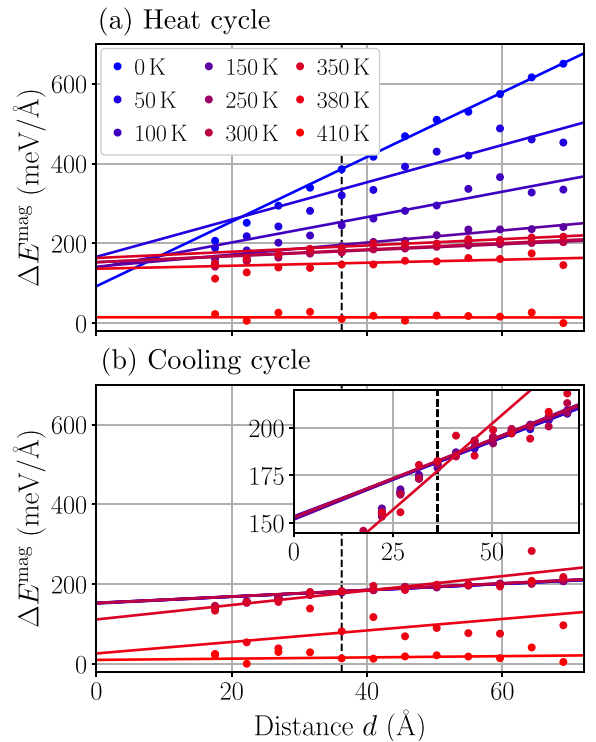


FIG. 10. Excess magnetic energy  $\Delta E^{\text{mag}}$  of the simulation cell containing a  $\frac{1}{2}(111)$  screw dislocation dipole as a function of  $d$  at various temperatures recorded upon (a) heating and (b) cooling the system.

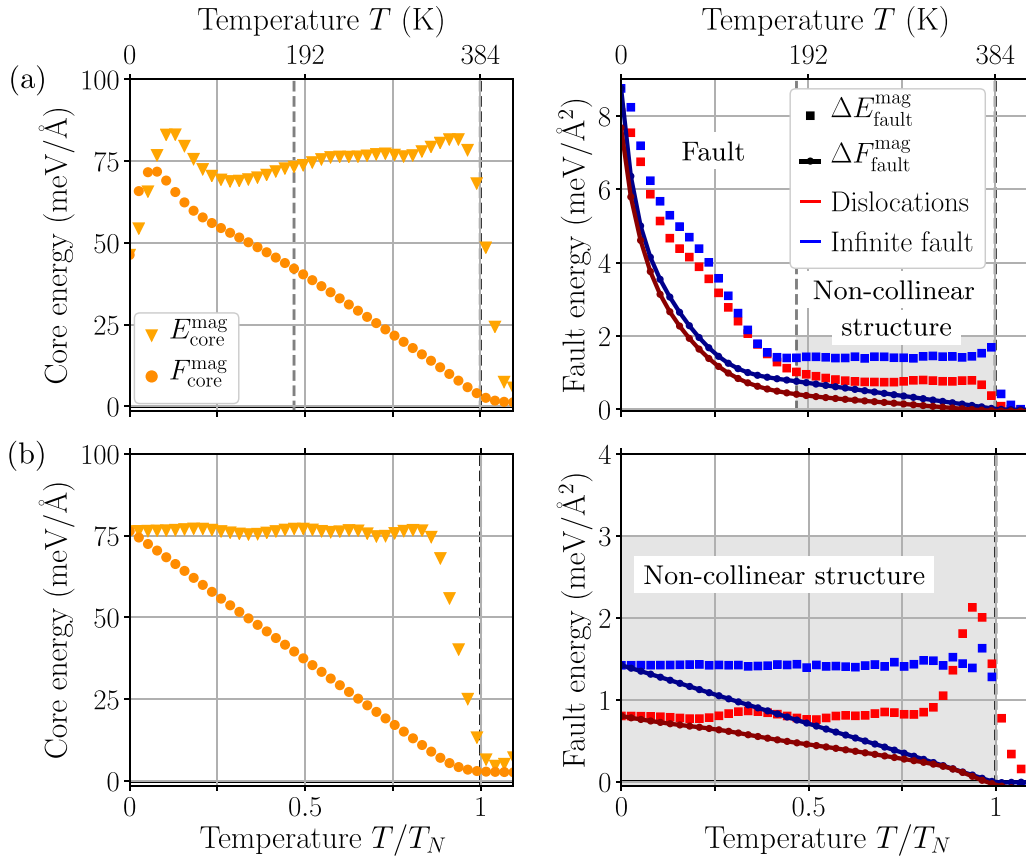


FIG. 11. (Left) Magnetic energy (triangles) and free energy (circles) of a  $\frac{1}{2}\langle 111 \rangle$  screw dislocation core as a function of temperature. (Right) Fault energy (squares) and free energy (circles) of the magnetic fault separating two  $\frac{1}{2}\langle 111 \rangle$  screw dislocations (in red), and compared to the infinite  $\{110\}$  fault of Fig. 5 (in blue). Simulations are performed with parameters Set2 of the HL model, upon (a) heating and (b) cooling the system.

magnetic energy and free energy of the fault show a similar temperature dependence as the infinite fault presented in the previous section and reported in blue on Fig. 11. Upon heating the system starting from 0 K, the magnetic fault is stable and located between the two dislocations of the simulation cell, up to approximately 180 K, with a linearly decreasing energy with temperature. When the temperature is increased, the noncollinear structure is stabilized by thermal fluctuations, with then a constant energy.

This noncollinear structure arises spontaneously upon cooling the system, with a constant magnetic energy across the whole temperature range, except near the Néel temperature  $T_N$  where fluctuations in the energy do not allow for a proper separation of the two contributions to the magnetic energy. Upon cooling through  $T_N$ , the slope of the total excess magnetic energy of the system given by Eq. (15) shows a sudden increase, before falling and then remaining constant down to 0 K with the same value as found upon heating the system between 180 K and  $T_N$ . Similar magnetic energy profiles with temperature, showing an increased energy near the disappearance of long-range magnetic order, has been previously reported in the case of domain walls in different systems [33].

Considering the magnetic contribution to the  $\frac{1}{2}\langle 111 \rangle$  screw dislocation core (left in Fig. 11), similar temperature variations are found upon heating and cooling the system, with

almost constant energy across the whole range of temperature below  $T_N$ , except near 0 K upon heating where this contribution falls. Due to the steep decrease of the magnetic fault energy, separation of the two contributions is difficult in this temperature range. This similar temperature dependence found whether heating or cooling shows that contrary to the fault, the core energy of the dislocations does not depend on the magnetic structure of the system. Like for the fault, the magnetic contribution to the core energy vanishes when long-range magnetic order disappears at  $T_N$ . This yields a linearly decreasing free energy with increasing temperature. As was previously reported using *ab initio* calculations [5], the magnetic contribution to the core energy of  $\frac{1}{2}\langle 111 \rangle$  screw dislocations at 0 K is very small, in agreement with the present results.

Looking at the results obtained upon cooling the infinite fault, the energy of the fault bounded by dislocations might also depend on the size of the simulation cell, with a similar noncollinear structure arising. To study this effect, similar simulations were performed using a smaller simulation cell, with periodicity vectors  $\vec{p}_1 = 15/2[\bar{1}2\bar{1}] - 27/2[\bar{1}01]$ ,  $\vec{p}_2 = 15/2[\bar{1}2\bar{1}] + 27/2[\bar{1}01]$ , and  $\vec{p}_3 = 6 \times \frac{1}{2}[111]$ , containing a total of 7 290 atoms. This corresponds to a distance of 54 Å between the two  $\frac{1}{2}[111]$  screw dislocations of the dipole when in its quadrupolar arrangement. The length of the sheared area is then varied as performed in the beginning of this



section to allow for the extraction of the contributions of the fault and dislocation cores to the total excess magnetic energy. Upon cooling the system, the magnetic contribution to the dislocation core energy at 0 K is 66 meV/Å, with a fault energy of 1.4 meV/Å<sup>2</sup>, compared to 76 meV/Å and 0.8 meV/Å<sup>2</sup>, respectively, in the larger cell presented above (see Fig. 11). The magnetic contribution to the core energy appears therefore almost constant for different sizes of the simulation cell, while the fault energy associated with the non-collinear structure strongly varies, in agreement with previous results obtained for infinite faulted crystals. This noncollinear structure shown in Fig. 9 therefore cannot be described as a fault since it is not localized in a defined fault plane, and its excess energy is not varying proportionally to the area of the fault plane. These noncollinear magnetic structures, however, have a lower energy than the ones involving collinear magnetic faults, thus corresponding to the magnetic ground state of the crystal containing a  $\frac{1}{2}\langle 111 \rangle$  screw dislocation dipole.

#### D. Dislocations and spin-density wave

As discussed in the Introduction, motivated by previous *ab initio* modeling of the interplay between 0-K magnetism and plasticity of Cr, all presented results in this work have been performed under the approximation of the AF phase. However, the experimental magnetic ground state of Cr at low temperature, the SDW, might have an effect on the discussed magnetic faults. Depending on the relative position between the location of the fault plane and the node of the wave, the situation might indeed differ. When the crystal is sheared in a {100} plane where all magnetic moments are zero, i.e., in a nodal plane of the SDW, the magnetic fault has zero energy since there is no magnetic frustration in the node where magnetic moments are null. However, since the  $\frac{1}{2}\langle 111 \rangle$  Burgers vector does not belong to {100} planes, such a shearing is not compatible with glide of  $\frac{1}{2}\langle 111 \rangle$  dislocations and the SDW order is necessarily broken in some of these {100} planes where magnetic moments are not zero. The SDW magnetic order will necessarily be disrupted, with a loss of the coherency between SDWs, in the same way as the AF order by  $\frac{1}{2}\langle 111 \rangle$  dislocations, responsible for the generation of magnetic faults.

To investigate this point, Monte Carlo simulations were performed in a simulation cell containing both a SDW and a  $\frac{1}{2}[111]$  screw dislocation dipole, the energetics of the system being described by Set1 parameters of the HL model. The system is sketched in Fig. 12(a), with periodicity vectors  $X = 20 \times [010]$ ,  $Y = 20 \times [101]$ , and  $Z = 9 \times [10\bar{1}]$ , containing 14 400 atoms. The SDW propagates along the  $x \parallel [010]$  axis, with a period of  $20a_0$ , chosen close to its experimental value [1]. The magnetic moments are initialized with  $m_i^x = m_i^y = 0$  and the  $m_i^z$  component as to match the profile of the SDW predicted by *ab initio* calculations at 0 K. In this configuration, the cut surface of the dislocation dipole necessarily cuts the SDW at any possible value of the magnetic moments along its [010] propagation direction.

The equilibrium magnetic structure of the system at 0 K is presented in Figs. 12(b) and 12(c). The position of the

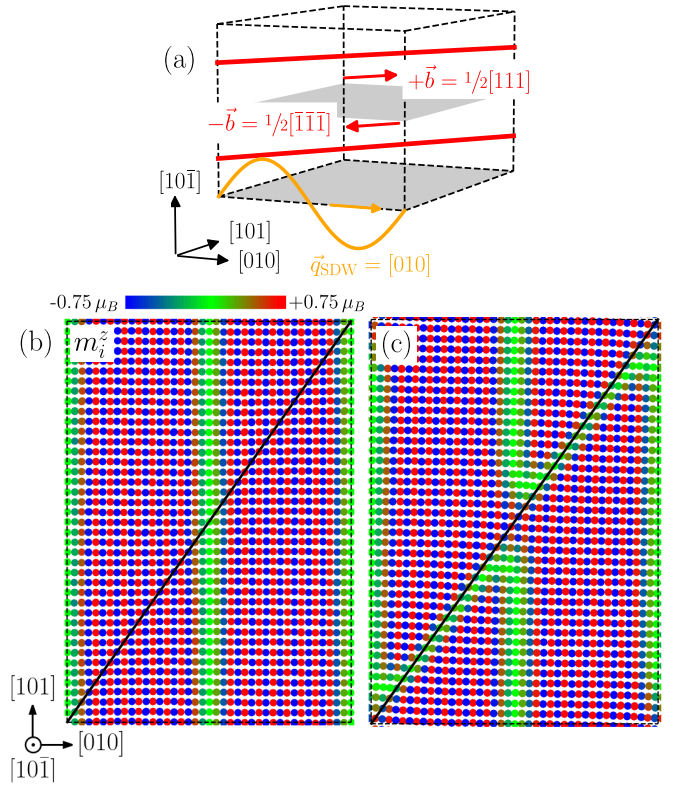


FIG. 12. (a) Sketch of the simulation setup containing a  $\frac{1}{2}[111]$  screw dislocation dipole and a SDW propagating along [010]. The projection of the magnetic moments along the  $z$  axis obtained at 0 K upon heating the system, using the HL model, is shown in the plane below the dislocation dipole in (b), and between the dislocations in (c), with the projected lines of the dislocations represented by the thick black line.

dipole defines two distinct regions: outside the sheared area [Fig. 12(b)], where the magnetic order is not disrupted; and between the two dislocations of the dipole [Fig. 12(c)], where a magnetic fault is generated. In the (010) planes corresponding to the nodes of the SDW located in the latter region, the shearing by the Burgers vector is canceled by the inversion of the magnetic ordering caused by the SDW, as shown in Fig. 12(c). Thus, AF order is retrieved in the region crossed by the cut surface of the dipole. In the (010) planes where the magnetic moments are nonzero, a collinear magnetic fault arises due to the disruption of the nonzero AF order, with a local reduction in the magnitude of the magnetic moments, as can be seen in Fig. 12(c) following the position of the dislocation lines (black line).

Upon increasing the temperature, both the SDW and the magnetic fault vanish, both below  $T_N$ , at the same temperature of approximately  $T_N/2$ . Now cooling the system down to 0 K starting from randomly oriented spins in the PM phase, a noncollinear structure is stabilized. It is similar to the one presented in Fig. 9, i.e., with a modulation of the three Cartesian components of the magnetic moments in the region sheared by the two  $\frac{1}{2}\langle 111 \rangle$  screw dislocations. Indeed, no SDW can be retrieved upon cooling since it is a metastable state of the HL model. Therefore, as in the AF phase, the  $\frac{1}{2}\langle 111 \rangle$  Burgers vector of these dislocations necessarily disrupt the

magnetic order, which is responsible for magnetic faults at low temperature. The AF phase is therefore *a priori* a good approximation to study the interplay between ordered magnetism and plasticity of bcc Cr at low temperature.

## V. DISCUSSION

In light of the presented results, the parameter governing the impact of magnetism on the plasticity of bcc Cr is the temperature, which defines if the magnetic fault caused by a  $\frac{1}{2}\langle 111 \rangle$  displacement is metastable. Above the transition temperature  $T_v$ , the magnetic fault is unstable. Magnetic faults created by the shearing of the crystal through glide of  $\frac{1}{2}\langle 111 \rangle$  dislocations will survive a time lapse defined by the relaxation time  $\tau_{\text{spin}}$  of the spins before relaxing to a noncollinear magnetic structure. If this time  $\tau_{\text{spin}}$  is large enough compared to the timescale associated with dislocation glide, one can still expect consequences of magnetism on plasticity, like back stress caused by magnetic faults, above  $T_v$ .

In this respect, we evaluate the magnetic excitation time  $\tau_{\text{spin}}$ , which is a measure of the timescale at which the spin subsystem relaxes to its equilibrium configuration. As roughly evaluated from the inverse of the weighted average of the magnon frequencies [34] of Fig. 3, we obtain  $\tau_{\text{spin}} = 19$  fs at 0 K, indicating the fast relaxation of the magnetic moments. On the other hand, dislocation motion typically operates at a timescale of the order of a few microseconds for the fastest motions [35]. The spin subsystem is thus always relaxed when considering the timescale of dislocation motion, and magnetic faults caused by the displacement of  $\frac{1}{2}\langle 111 \rangle$  dislocations instantly vanish in favor of their noncollinear ground state. Therefore, if the temperature of the system raises above  $T_v$ , all magnetic faults previously generated will vanish, regardless of the heating or cooling thermal cycle, and  $\frac{1}{2}\langle 111 \rangle$  dislocations are free to move without dragging a magnetic fault, surrounded by a noncollinear magnetic structure similar to the one presented in Fig. 9. In this temperature range, magnetism will not bear significant consequences on the plasticity of bcc Cr since the faults have disappeared.

Magnetic faults might only exist at low temperatures, below the transition temperature  $T_v$ . In this temperature range, one can expect that  $\frac{1}{2}\langle 111 \rangle$  dislocations glide pairwise, with the trailing dislocation closing the magnetic fault opened by the leading one, thus creating  $\langle 111 \rangle$  superdislocations [4,5]. Using the free energy  $\gamma_{\text{fault}}$  of the magnetic fault bounded by the two  $\frac{1}{2}\langle 111 \rangle$  screw dislocations (Fig. 11, right), the equilibrium dissociation distance of the  $\langle 111 \rangle$  screw superdislocation is evaluated with anisotropic elasticity (see details in Ref. [5]):

$$d_{\text{diss}}(T) = \frac{b^2 \sqrt{C' C_{44}}}{2\pi \gamma_{\text{fault}}(T)}, \quad (16)$$

using the low-temperature experimental shear moduli  $C' = 153$  and  $C_{44} = 104$  GPa [36]. The resulting dissociation distance is presented in Fig. 13 as a function of the temperature  $T$  upon heating the system up to 180 K, i.e., in the temperature range where the magnetic fault is metastable. The dissociation distance rapidly increases up to a few hundreds of nanometers, even at very low temperatures.

However, no such superdislocation seems to have been observed experimentally until now. Nevertheless, if the existence

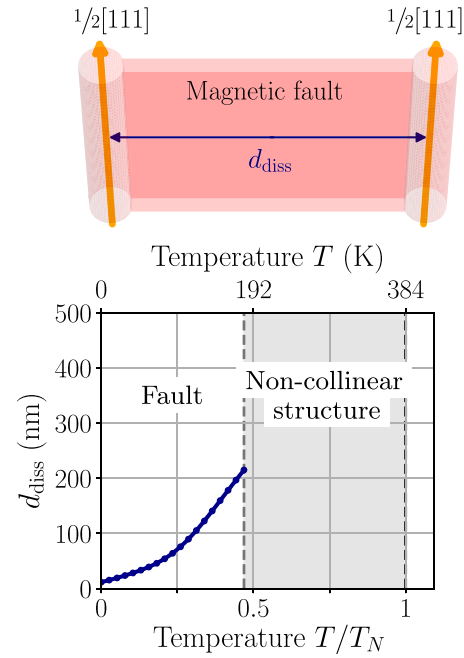


FIG. 13. Dissociation distance  $d_{\text{diss}}$  [Eq. (16)] of a  $\langle 111 \rangle$  screw superdislocation as a function of temperature, sketched in the above panel.

of dissociated  $\langle 111 \rangle$  superdislocations is to be confirmed, a careful experimental procedure is required. *Post mortem* imaging at room temperature of the dislocation microstructure present after low-temperature deformation will not allow for their observation since the magnetic faults will not be stable anymore. Maintaining the temperature below  $T_v$  all along the straining experiments and the observation step is necessary to allow for the detection of such superdislocations without destabilizing them. *In situ* straining experiments in a TEM at a temperature below  $T_v$  could be a possibility.

Various experimental works [37–40] report signatures of magnetic frustrations using spin-polarized STM at room temperature. In particular, pairs of  $\frac{1}{2}\langle 111 \rangle$  screw dislocations have been observed emerging at  $\{100\}$  surfaces, responsible for monoatomic steps of height  $a_0/2$  (i.e., the projection of  $\vec{b} = \frac{1}{2}\langle 111 \rangle$  along a  $\langle 100 \rangle$  direction), with  $a_0$  the lattice parameter. The variation of the magnetic contrast imaged in the region close to these dislocations shows the presence of magnetic domain walls bounded by two dislocations, of width of a few hundred nanometers. Since these observations were performed at room temperature, the magnetic fault generated by  $\frac{1}{2}\langle 111 \rangle$  dislocations has disappeared. The observed modulation in the magnetic contrast in the region between the two dislocations might therefore be an image of the noncollinear structure presented in Fig. 9.

## VI. CONCLUSION

The effect of finite-temperature magnetic excitations on different bulk and plasticity-related magnetic properties of bcc Cr is studied using a Heisenberg-Landau magnetic interaction model parametrized on *ab initio* data. Two different sets of parameters are used, one reproducing perfectly 0-K energetics

and the other the experimental Néel temperature  $T_N$ , then allowing for sampling of magnetic structures at finite temperatures, taking care of quantum statistics at low temperature. The bulk magnetization, short-range magnetic correlations and loss of long-range order at  $T_N$  are well captured by the model, in agreement with experiments.

Considering the magnetic frustration caused by a rigid  $\frac{1}{2}\langle 111 \rangle$  shearing of the lattice, we showed that the low-temperature collinear magnetic fault, where the magnetic frustration is partially resolved by a local reduction of the magnetic moments, is only stable up to a temperature  $T_v$ , which is below  $T_N$  (approximately  $2T_N/3$ ). Above  $T_v$ , the magnetic frustration is partially resolved by a disorientation of the magnetic moments, keeping a constant magnitude, a structure similar to a spin spiral. This perturbation spreads over the entire simulated volume, with zero excess magnetic energy in the limit of infinitely long simulation cells. Upon cooling the same system from the PM phase, this spiral structure is stabilized as soon as long-range magnetic order is retrieved at  $T_N$ , down to 0 K. The stability of these two magnetic structures, the collinear magnetic fault and the noncollinear spiral-like structure, predicted by the HL model were then confirmed by noncollinear *ab initio* calculations, the spiral structure being the ground state of the sheared crystal at all temperatures.

When the crystal is sheared by  $\frac{1}{2}\langle 111 \rangle$  dislocations, the same collinear magnetic fault is found in the region bounded by two dislocations up to the temperature  $T_v$ , below  $T_N$ . In this temperature range, a possible consequence of the non-negligible energy cost of these magnetic faults is the pairing of  $\frac{1}{2}\langle 111 \rangle$  dislocations, creating dissociated  $\langle 111 \rangle$  superdislocations [4]. Upon increasing the temperature, the fault progressively vanishes, with a rapid decrease in the magnetic free energy of the fault and thus the disappearance of dislocation pairing. Above  $T_v$ , a noncollinear structure spreading over the whole simulation cell is obtained, similar to the spiral-like structure previously found for the rigid  $\frac{1}{2}\langle 111 \rangle$  shearing of the lattice. This noncollinear structure has a negligible excess magnetic energy, and  $\frac{1}{2}\langle 111 \rangle$  dislocations are thus free to move without carrying any magnetic fault above  $T_v$ .

In its magnetically ordered phase above the transition temperature  $T_v$  at which magnetic faults vanish, but also in its disordered PM phase above the Néel temperature  $T_N$ , magnetism appears to have a marginal impact on Cr plasticity. Indeed, previous *ab initio* results at 0 K have shown that dislocations have similar core properties in the nonmagnetic and antiferromagnetic phases [5,6], the only notable difference being the generation of magnetic faults by  $\frac{1}{2}\langle 111 \rangle$  dislocations at 0 K. Once these magnetic faults have become unstable above  $T_v$ , magnetism should not have any consequence on Cr plasticity. A plastic behavior similar to other bcc transition metals is therefore expected for Cr [41].

## ACKNOWLEDGMENTS

This work was performed using HPC resources from GENCI-IDRIS and TGCC (Grant No. 2022-096847). The authors acknowledge funding by the French Tripartite Institute (CEA-EDF-Framatome) through the ICOMB project.

## APPENDIX A: INCLUDING QUANTUM STATISTICS

Magnetic excitations described by the HL model are assumed continuous in the frame of classical physics, thus allowing for fluctuations in the magnitude and angle of the spins even at very low temperatures, as soon as thermal energy is sufficient to explore higher-energy configurations. However, this yields nonphysical results with a diverging magnetic entropy at 0 K [26]. This can be overcome using a quantum statistics through the inclusion of quantized excitation modes, or magnons, as presented in Fig. 3(a), which then allow for a better description of low-temperature magnetic excitations.

A proper sampling of the thermodynamic properties of the system therefore necessitates quantum statistics, i.e., using a Bose-Einstein distribution. The quantum scaling factor  $\eta(T)$  of the Metropolis algorithm is given by Eq. (7), obtained through integration of the temperature-dependent magnon density of states (mDOS)  $g(E, T)$ , which is then the key to construct such quantum statistics [26]. Given that the mDOS is zero above a certain maximum energy, approximately 625 meV/atom according to the HL model with Set1 parameters [Fig. 3(a)], one can perform this integration from 0 to  $E_C$ , where  $E_C$  is the highest energy contributing to the mDOS at a temperature  $T$ . Following the method introduced by Woo *et al.* [27] and Bergqvist *et al.* [26], the temperature dependence of the mDOS is evaluated by rescaling this upper limit in energy  $E_C$  of the mDOS at 0 K following

$$E_C(T) = E_C(T = 0 \text{ K}) \times \left(1 - \frac{T}{T_N}\right)^\beta, \quad (\text{A1})$$

with  $T_N$  the Néel temperature and  $\beta \simeq 0.375$  the critical exponent of the three-dimensional (3D) Heisenberg model [42], which only depends on the dimensionality of the model and is the same regardless of the structure of the system of interest. This implies that the temperature-dependent mDOS is rescaled upon temperature, keeping the same shape with this rescaled cutoff magnon energy (Fig. 14):

$$g(E, T) = \frac{g\left(E \times \frac{E_C(T)}{E_C(0 \text{ K})}, 0 \text{ K}\right)}{\int_{e=0}^{E_C(T)} g\left(e \times \frac{E_C(T)}{E_C(0 \text{ K})}, 0 \text{ K}\right) de}. \quad (\text{A2})$$

This model assumes that above  $T_N$ , i.e., when long-range magnetic order vanishes, the cutoff energy  $E_C$  becomes zero and the statistics thus sharply switches from quantum to classical. Hence, such an approximation is exact at low temperatures only, well below  $T_N$ , but still a reasonable approximation at higher temperatures, close to  $T_N$ , as demonstrated in previous works [13,43,44]. This method is applied with the magnon spectrum obtained with a given energetic model, from which the mDOS at 0 K is obtained by integrating the energy of the magnons over the entire Brillouin zone. The scaling factor  $\eta$  of the Metropolis algorithm is then interpolated at the transition from classical to quantum statistics:

$$\eta(T) = \begin{cases} \eta_Q(T) [\text{Eq. (7)}], & \text{if } T < T_N \\ k_B T, & \text{if } T \geq T_N \end{cases} \quad (\text{A3})$$



correctly accounting for low-temperature thermal excitations below the Néel temperature  $T_N$  through quantum statistics, and using a classical Boltzmann distribution above, which is presented in the middle column of Fig. 14. We note that a more accurate evaluation of the temperature-dependent mDOS can be obtained through evaluation of the dynamical structure factor  $S(\vec{q}, E)$  [45–47], including temperature effects originating from magnon-magnon interactions and magnetic damping. However, this approach is much more computationally expensive and yields a similar scaling factor at low temperature as the quantum approximation introduced in this section. Thus, finite-temperature magnetic excitations in bcc Cr are studied using the statistics of Eq. (A3), which gives a better agreement with the experimental measure of the long-range magnetic order than using classical statistics, as presented in the right column of Fig. 14. We also note that similar results are obtained using the two sets of parameters for the HL model, with only a shift in the temperature scale due to the different predicted  $T_N$ .

## APPENDIX B: NONCOLLINEAR SPIN-POLARIZED DFT CALCULATIONS

In order to confirm the predictions of the HL model regarding the stability and energetics of the two magnetic structures presented in Fig. 6 (i.e., the collinear magnetic fault and the noncollinear spiral structure), noncollinear spin-polarized

DFT calculations are performed. The simulation cells used for the {110} fault has periodicity vectors  $\vec{x} = [010]$ ,  $\vec{y} = [101]$ , and  $\vec{z} = n_{\{110\}} \times [10\bar{1}] + 1/2[111]$ , with  $n_{\{110\}} \in [6, 8, 14]$ , resulting in a length  $d_{\text{cell}}^{\{110\}} = n_{\{110\}} \times a_0\sqrt{2}$  in the direction orthogonal to the fault plane. For the {112} fault, the simulation cell has periodicity vectors  $\vec{x} = [\bar{1}10]$ ,  $\vec{y} = \frac{1}{2}[111]$ , and  $\vec{z} = 4 \times [11\bar{2}]$ , resulting in  $d_{\text{cell}}^{\{112\}} = 4 \times a_0\sqrt{6}$ . The magnetic moments are then initialized using their equilibrium values obtained with the HL model. The *ab initio* relaxed structures are presented in Fig. 6 for the infinite {110} structure, both found identical to the predictions of the HL model. The energies of both structures are presented in Fig. 7 as a function of the separation distance  $d_{\text{cell}}$  at 0 K, in both {110} and {112} planes, also confirming the predictions of the HL model.

Calculations of the energy of magnons (Fig. 3) have been performed using both DFT and the TB formalism using the generalized Bloch's theorem [19], as implemented in the VASP [8] and DYNAMOL [20] codes, respectively. Spin spirals of wave vector  $\vec{q}$  are propagating in a bcc unit cell containing a single atom, with periodicity vectors  $\vec{p}_1 = \frac{1}{2}[\bar{1}11]$ ,  $\vec{p}_2 = \frac{1}{2}[1\bar{1}1]$ , and  $\vec{p}_3 = 1/2[11\bar{1}]$ . These noncollinear calculations are performed at the equilibrium lattice parameter of the AF phase, with a magnetic moment constrained to the bulk value  $m_0$  of the AF phase, since magnons are noncollinear spirals keeping a constant magnetic moment along their propagation direction. The results are presented in Fig. 3, using DFT calculations (orange circles) and the TB model (gray line).

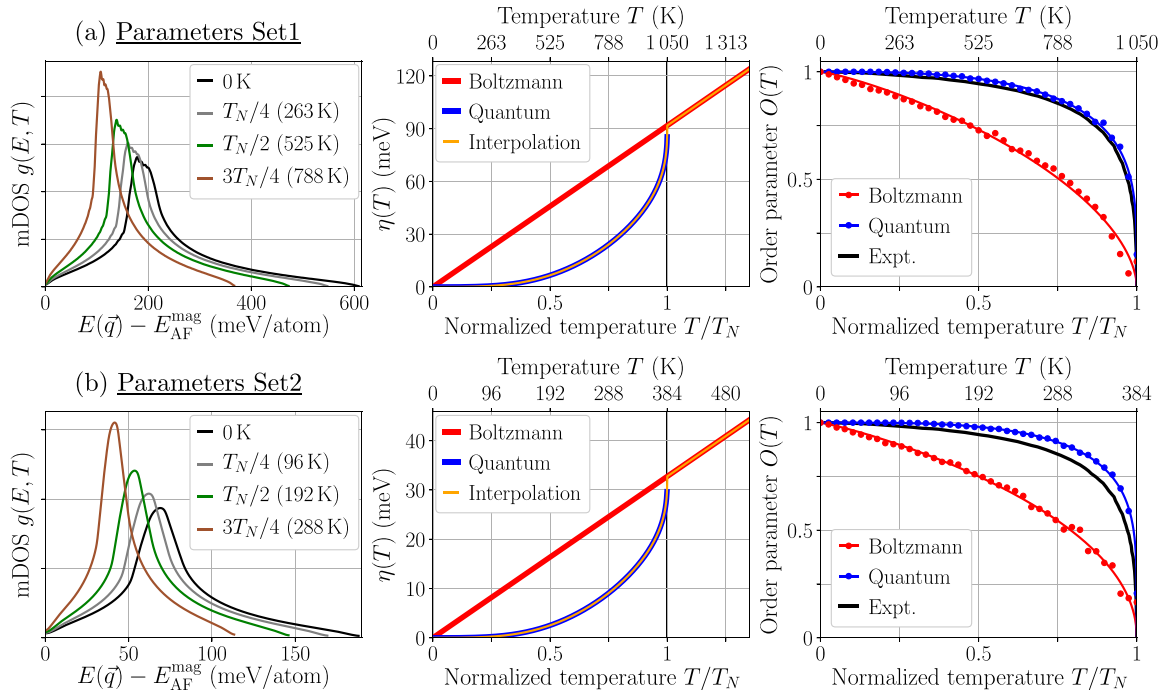


FIG. 14. Temperature-dependent mDOS  $g(E, T)$ , scaling factor of the Metropolis algorithm  $\eta(T)$  within the classical Boltzmann (red) quantum statistics (blue), and long-range magnetic order  $O$  [Eq. (12)] as a function of temperature using both statistics, and compared to experiments [1]. Results are presented for (a) Set1 and (b) Set2 parameters of the HL model.

- [1] E. Fawcett, *Rev. Mod. Phys.* **60**, 209 (1988).
- [2] G. E. Bacon and N. Cowlam, *J. Phys. C: Solid State Phys.* **2**, 238 (1969).
- [3] I. S. Williams and R. Street, *Philos. Mag. B* **43**, 893 (1981).
- [4] M. J. Marcinkowski and H. A. Lipsitt, *Acta Metall.* **10**, 95 (1962).
- [5] B. Bienvenu, C. C. Fu, and E. Clouet, *Acta Mater.* **200**, 570 (2020).
- [6] B. Bienvenu and E. Clouet, *Acta Mater.* **224**, 117485 (2022).
- [7] J. Holzer, Z. Chlup, T. Kruml, and R. Gröger, *Int. J. Plast.* **138**, 102938 (2021).
- [8] G. Kresse and J. Furthmüller, *Comput. Mater. Sci.* **6**, 15 (1996).
- [9] J. P. Perdew, K. Burke, and M. Ernzerhof, *Phys. Rev. Lett.* **77**, 3865 (1996).
- [10] R. Hafner, D. Spišák, R. Lorenz, and J. Hafner, *Phys. Rev. B* **65**, 184432 (2002).
- [11] S. Cottenier, B. D. Vries, J. Meersschant, and M. Rots, *J. Phys.: Condens. Matter* **14**, 3275 (2002).
- [12] R. Soulaïrol, C.-C. Fu, and C. Barreateau, *J. Phys.: Condens. Matter* **22**, 295502 (2010).
- [13] A. Schneider, Corrélations entre le magnétisme, la thermodynamique et la diffusion dans les alliages Fe-Mn cubiques centrés: Des premiers principes aux températures finies, Ph.D. thesis, Université Paris-Saclay, 2019.
- [14] M. Y. Lavrentiev, D. Nguyen-Manh, and S. L. Dudarev, *Comput. Mater. Sci.* **49**, S199 (2010).
- [15] F. Ducastelle, *Interatomic Potential and Structural Stability*, Springer Series in Solid-State Sciences (Springer, Berlin, 1993), pp. 133–142.
- [16] M. A. Ruderman and C. Kittel, *Phys. Rev.* **96**, 99 (1954).
- [17] W. Setyawan and S. Curtarolo, *Comput. Mater. Sci.* **49**, 299 (2010).
- [18] S. Shallcross, A. E. Kissavos, V. Meded, and A. V. Ruban, *Phys. Rev. B* **72**, 104437 (2005).
- [19] L. M. Sandratskii, *Adv. Phys.* **47**, 91 (1998).
- [20] C. Barreateau, D. Spanjaard, and M.-C. Desjonquères, *C. R. Phys.* **17**, 406 (2016).
- [21] R. Soulaïrol, C.-C. Fu, and C. Barreateau, *Phys. Rev. B* **84**, 155402 (2011).
- [22] R. Soulaïrol, C. Barreateau, and C.-C. Fu, *Phys. Rev. B* **94**, 024427 (2016).
- [23] D. G. Van Campen, M. L. Knieriem, and L. E. Klebanoff, *Phys. Rev. B* **43**, 11668 (1991).
- [24] X. Wu, Z. Liu, and T. Luo, *J. Appl. Phys.* **123**, 085109 (2018).
- [25] S. A. Werner, A. Arrott, and H. Kendrick, *Phys. Rev.* **155**, 528 (1967).
- [26] L. Bergqvist and A. Bergman, *Phys. Rev. Mater.* **2**, 013802 (2018).
- [27] C. H. Woo, H. Wen, A. A. Semenov, S. L. Dudarev, and P.-W. Ma, *Phys. Rev. B* **91**, 104306 (2015).
- [28] B. H. Grier, G. Shirane, and S. A. Werner, *Phys. Rev. B* **31**, 2892 (1985).
- [29] R. Przeniosło, P. Fabrykiewicz, I. Sosnowska, D. Wardecki, W. A. Sławiński, H. Y. Playford, R. Hempelmann, and M. Bukowski, *Phys. B (Amsterdam)* **530**, 183 (2018).
- [30] E. Fawcett, *Phys. B (Amsterdam)* **180-181**, 179 (1992).
- [31] K. R. A. Ziebeck, J. G. Boom, P. J. Brown, H. Capellmann, and J. A. C. Bland, *Z. Phys. B* **48**, 233 (1982).
- [32] D. Rodney and J. Bonneville, in *Physical Metallurgy (Fifth Edition)* (Elsevier, Amsterdam, 2014), pp. 1591–1680.
- [33] D. Hinzke, N. Kazantseva, U. Nowak, O. N. Mryasov, P. Asselin, and R. W. Chantrell, *Phys. Rev. B* **77**, 094407 (2008).
- [34] B. L. Gyorffy, A. J. Pindor, J. Staunton, G. M. Stocks, and H. Winter, *J. Phys. F: Met. Phys.* **15**, 1337 (1985).
- [35] D. Caillard, *Acta Mater.* **58**, 3493 (2010).
- [36] S. B. Palmer and E. W. Lee, *Philos. Mag.* **24**, 311 (1971).
- [37] R. Ravlić, M. Bode, A. Kubetzka, and R. Wiesendanger, *Phys. Rev. B* **67**, 174411 (2003).
- [38] J. Lagoute, S. L. Kawahara, C. Chacon, V. Repain, Y. Girard, and S. Rousset, *J. Phys.: Condens. Matter* **23**, 045007 (2011).
- [39] M. Kleiber, M. Bode, R. Ravlić, and R. Wiesendanger, *Phys. Rev. Lett.* **85**, 4606 (2000).
- [40] M. Kleiber, M. Bode, R. Ravlić, N. Tezuka, and R. Wiesendanger, *J. Magn. Magn. Mater.* **240**, 64 (2002).
- [41] B. Bienvenu, L. Dezerald, D. Rodney, and E. Clouet, *Acta Mater.* **236**, 118098 (2022).
- [42] L. P. Kadanoff, W. Göetze, D. Hamblen, R. Hecht, E. A. S. Lewis, V. V. Palciauskas, M. Rayl, J. Swift, D. Aspnes, and J. Kane, *Rev. Mod. Phys.* **39**, 395 (1967).
- [43] K. Li, Magnetochemical coupling effects on thermodynamics, point-defect formation and diffusion in Fe-Ni alloys: a theoretical study, Ph.D. thesis, Université Paris-Saclay, 2021.
- [44] A. Schneider, C.-C. Fu, F. Soisson, and C. Barreateau, *Phys. Rev. Lett.* **124**, 215901 (2020).
- [45] C. Etz, L. Bergqvist, A. Bergman, A. Taroni, and O. Eriksson, *J. Phys.: Condens. Matter* **27**, 243202 (2015).
- [46] A. Bergman, A. Taroni, L. Bergqvist, J. Hellsvik, B. Hjörvarsson, and O. Eriksson, *Phys. Rev. B* **81**, 144416 (2010).
- [47] L. Bergqvist, A. Taroni, A. Bergman, C. Etz, and O. Eriksson, *Phys. Rev. B* **87**, 144401 (2013).